1/
5-23-76

SAND75-0426
Unlimited Release
Autumn 1975

25 NTIS

SANDIA TECHNOLOGY

MASTER

Sandia Laboratories

F 2900 Q(7-73)

DISTRIBUTION OF THIS DOCUMENT IS UNLI

Printed in the United States of America

Available from
National Technical Information Service
U. S. Department of Commerce
5285 Port Royal Road
Springfield, Virginia 22151

Price: Printed Copy $5.00; Microfiche $2.25

Contents

Electric Contact Arcing – p. 4
R. E. Cuthrell
Electrical contacts may be damaged by arcing that precedes closure at voltage levels commonly used in component test evaluation.

Development of Materials for Hydrogen Storage and Transport – p. 8
J. A. Brooks, A. J. West
Thermo-mechanical processing or slight modification of chemical composition can improve the ability of steels to resist failure in hydrogen environments.

Measurement of Thermal Transients – p. 15
N. R. Keltner
With thermal sensor response models we can improve the accuracy of measurements from transient thermal experiments.

Lithium Niobate Stress Transducers – p. 19
R. A. Graham
Determination of piezoelectric characteristics of lithium niobate has led to development of new transducers for measuring fast, high-level stress pulses.

Stability of Liquid Films in Transpiration-Cooling – p. 24
W. S. Saric, K. J. Touryan
Stability characteristics of liquid films on transpiration-cooled hypersonic vehicles can be predicted by analytical models.

Accident-Resistant Containers for Nuclear Weapons – p. 28
R. E. Berry
To prevent detonation of high explosives in accidents during transportation of nuclear weapons, we have developed a practical technology for design of accident-resistant containers.

Metrication – Inside back cover

SAND75-0426

Sandia Technology

Sandia Laboratories

Autumn 1975

Published February 1976

John Weber, *Technical Editor*
Phil Mead, *General Editor*

foreword

This report describes significant development activities of Sandia Laboratories in discharging its responsibilities to the Energy Research and Development Administration, and conducting projects for other agencies. Activities of a classified nature are reported in the Technical Review, the other quarterly technical publication of Sandia Laboratories.

Electric Contact Arcing

Electrical contacts may be damaged by arcing that precedes closure at voltage levels commonly used in component test evaluation.

R. E. Cuthrell

Introduction

Electrical contacts must function properly in many types of components used in nuclear weapon systems. Design, application, and testing of these components requires detailed knowledge of chemical and physical phenomena associated with stockpile storage, stockpile testing, and operation. In the past, our investigation of these phenomena has led to significant discoveries on the effects of surface contaminants, friction and wear, and the mechanics of closure on contact performance. In this article we will describe a recent investigation of contact arcing phenomena which revealed that, preceding contact closure, arcs may occur at voltages lower than had been previously known.

This discovery is important, since arcing may damage contacts, and repetitive testing of contacts performed as part of a quality assurance program might produce cumulative damage that would yield misleading life-test data and could prevent proper operation of the contacts at some time in the future. This damage can be avoided by determining the conditions under which arcing occurs, and ensuring that these conditions are avoided in contact testing.

Contact Arcing

It is well known that opening of contacts in an electrical circuit may result in an arc between the contacts. Likewise, if a contact bounces after initial closure, an arc may form. In both cases current flowing between the closed contacts results in joule heating of the last area in contact, which causes melting and vaporization of a metallic bridge and formation of an arc as the contacts separate. On the other hand, when contacts approach each other, arcing is generally not expected prior to closure unless the potential difference is quite high.

Melting and boiling of contact materials have been observed by many investigators at voltages much lower than the commonly accepted "minimum arcing voltages" (i.e., lower than 11 to 15 volts). Melting and boiling voltages of contact materials have been found to be well-defined characteristics of the material, due to a relationship between voltage drop in a current path constriction, and temperature increase caused by joule heating. For most contact materials, melting and boiling voltages are less than one volt.

Since for closing contacts it is possible for contact material melting and boiling to occur at low voltage levels, and since the metallic vapor is a prerequisite for some types of arcing, it appears possible that contact arcing may be initiated at low voltages. For these reasons we decided to conduct experiments with common contact materials to determine whether arcing does occur at applied voltages lower than the oft-cited "minimum arcing voltages."

Experiments

Electrical and optical measurements were made as electrical contacts were slowly closed with the apparatus shown in Fig. 1. The fixture was made very rigid and mounted on vibration isolators to prevent any uncontrolled relative motion between the contacts. The very sensitive piezoelectric micrometer provided slow, accurate contact displacement by bending the cantilever arm at about 50 µm/s. Typical contact closure rates between 0.05 and 0.5 m/s were also investigated. Displacement was proportional to the voltage applied to the piezoelectric element. Voltage across the contacts and current during closure were monitored with the circuit shown in Fig. 2.

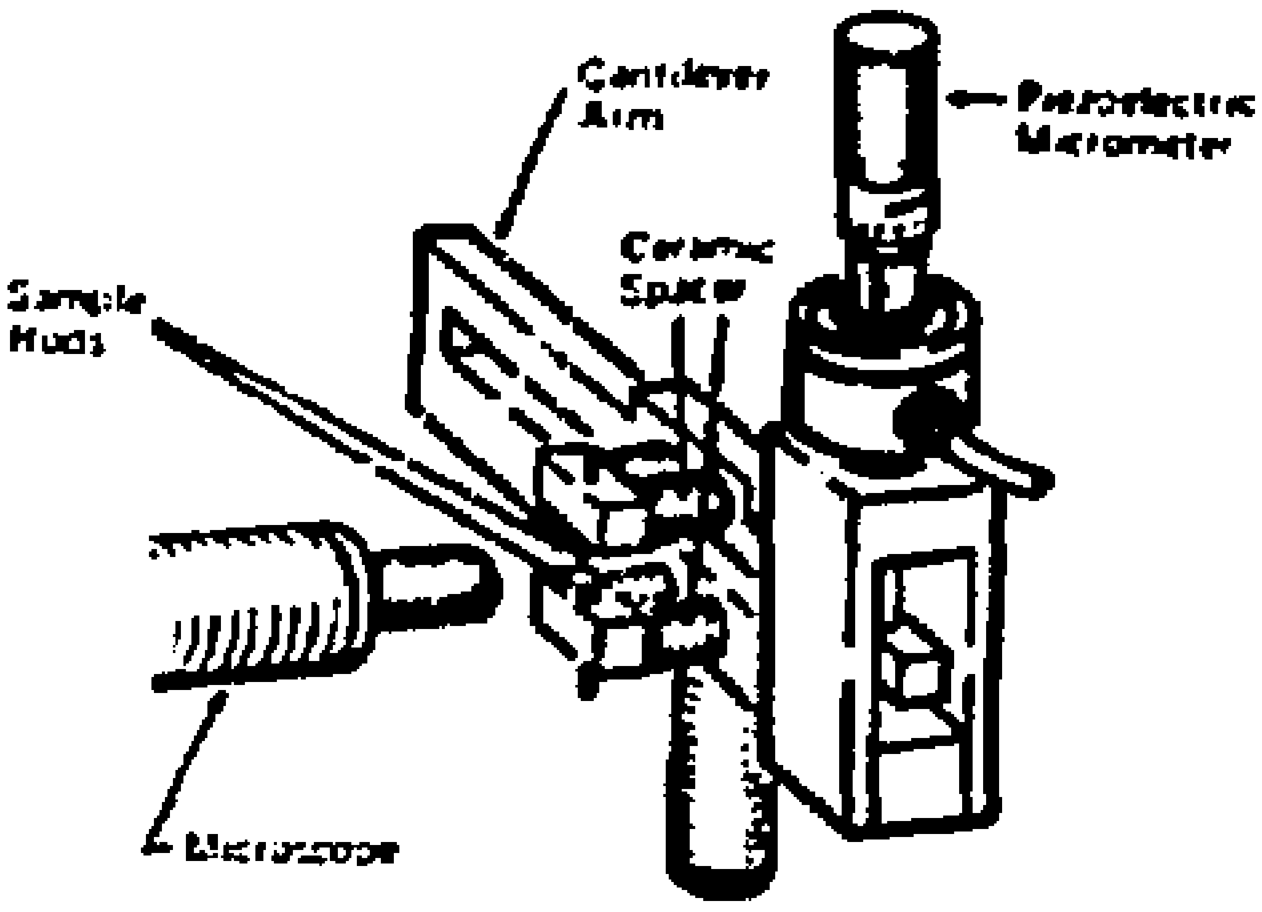

Fig. 1 Contact closure studies were conducted with a very rigid fixture in which precise closure was provided by a piezoelectric micrometer.

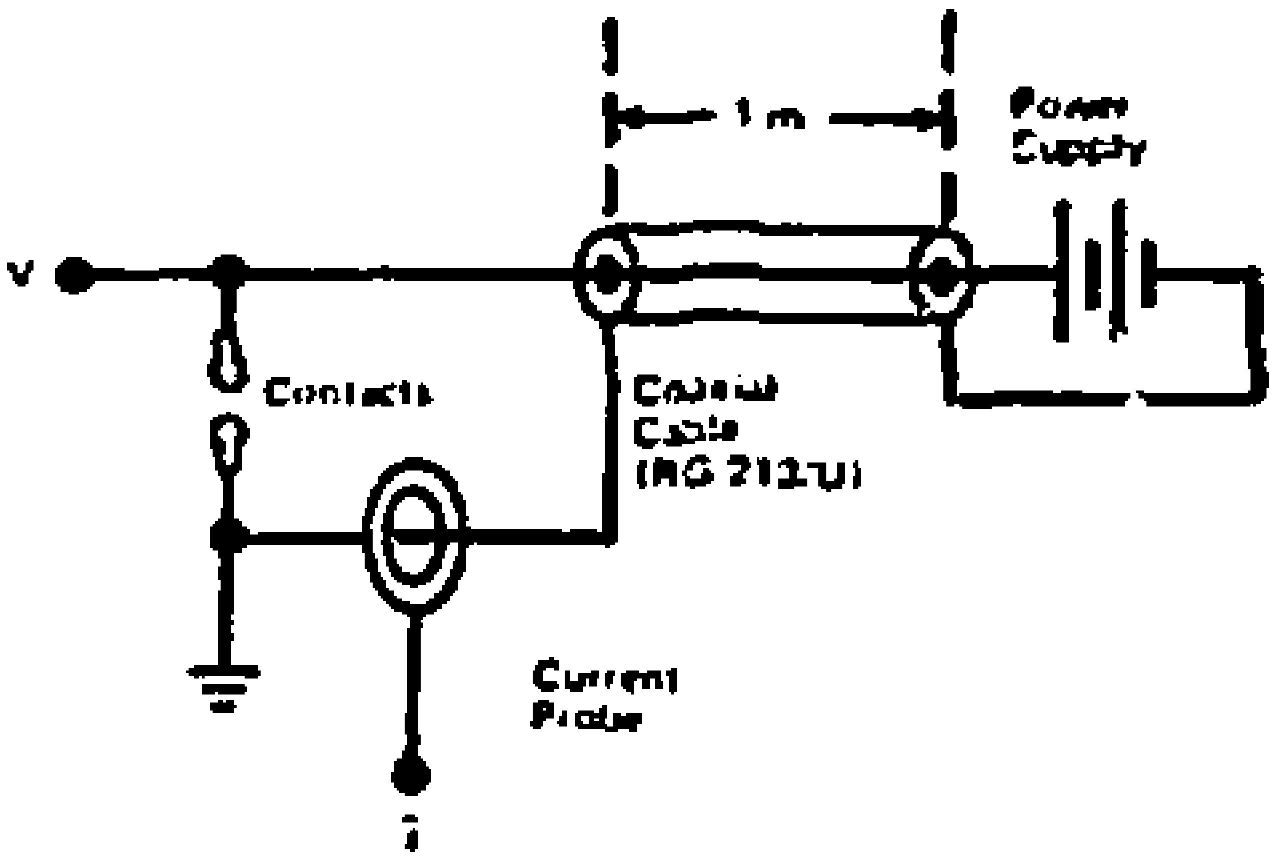

Fig. 2 Potential across contacts and current were recorded with oscilloscope cameras as contacts were closed.

Contact materials studied included copper, tungsten, silver, aluminum, iron, molybdenum, nickel, platinum, and gold. Extremely smooth gold contacts were prepared by quenching from the melt. Some of these were repetitively arced to produce controlled surface roughness. Except for gold and platinum, the metals oxidize rapidly in air (increasing voltage standoff); therefore fresh surfaces were prepared just prior to testing by cutting off the ends of rods.

Results

When roughened gold contacts with a potential difference of 6 volts were closed, it was found that transient voltage and current pulses often preceded firm closure. Figure 3a shows an oscilloscope trace which was triggered by a voltage transient that occurred 29 ms before firm closure. These transients were too fast to be recorded at the sweep speed used for Fig. 3a, and are shown at higher sweep speeds in Figs. 3b and 3c. These traces showed a fast drop in potential, then a slow rise, followed by a rapid, inductively generated increase to create the arcing voltage. Since *there were no indications of firm contact on this short time* scale, it appeared that the behavior could best be explained in terms of an asperity making initial contact, melting, and vaporizing to form a momentary arc prior to firm closure.

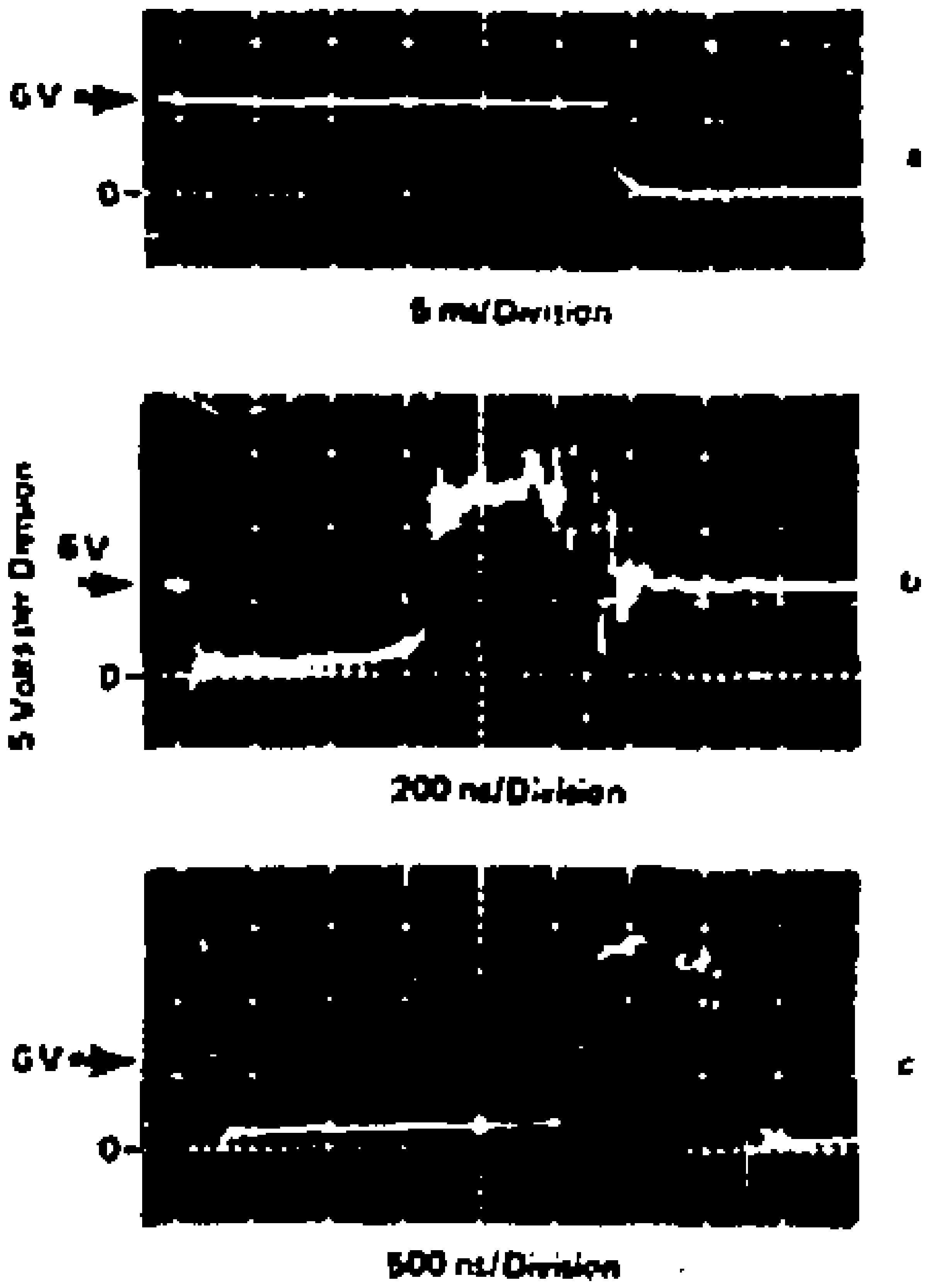

Fig. 3 Oscilloscope traces of the potential across closing gold contacts at 6 V open-circuit potential. The upper trace, which was triggered by events such as those shown in the lower two photographs, shows the potential drop at the firm closure of the solid contacts with no indications of contact bounce. The two lower traces show the drop in potential associated with asperity contacting, the slow rise in potential as joule heating occurs, and the rapid increase to the arcing voltage which may occur when the asperity contact is pinched off by magnetic forces. Note that the post-arc condition may be a transient open-circuit or closed-circuit condition.

Tests revealed that transients indicative of arcing prior to closure could be obtained with all types of contact materials at open circuit voltage levels only slightly above the melting voltage. Microscopic observation confirmed that arcing did occur. Figure 4 shows photographs of arcs obtained at low voltages with copper and gold contacts. Examination of contacts after testing also showed surface damage which is characteristic of arcing (Fig. 5). Table I summarizes the results of this study, showing the minimum arc initiation voltage that was determined for each contact material, as well as the melting and boiling voltages determined by other investigators.

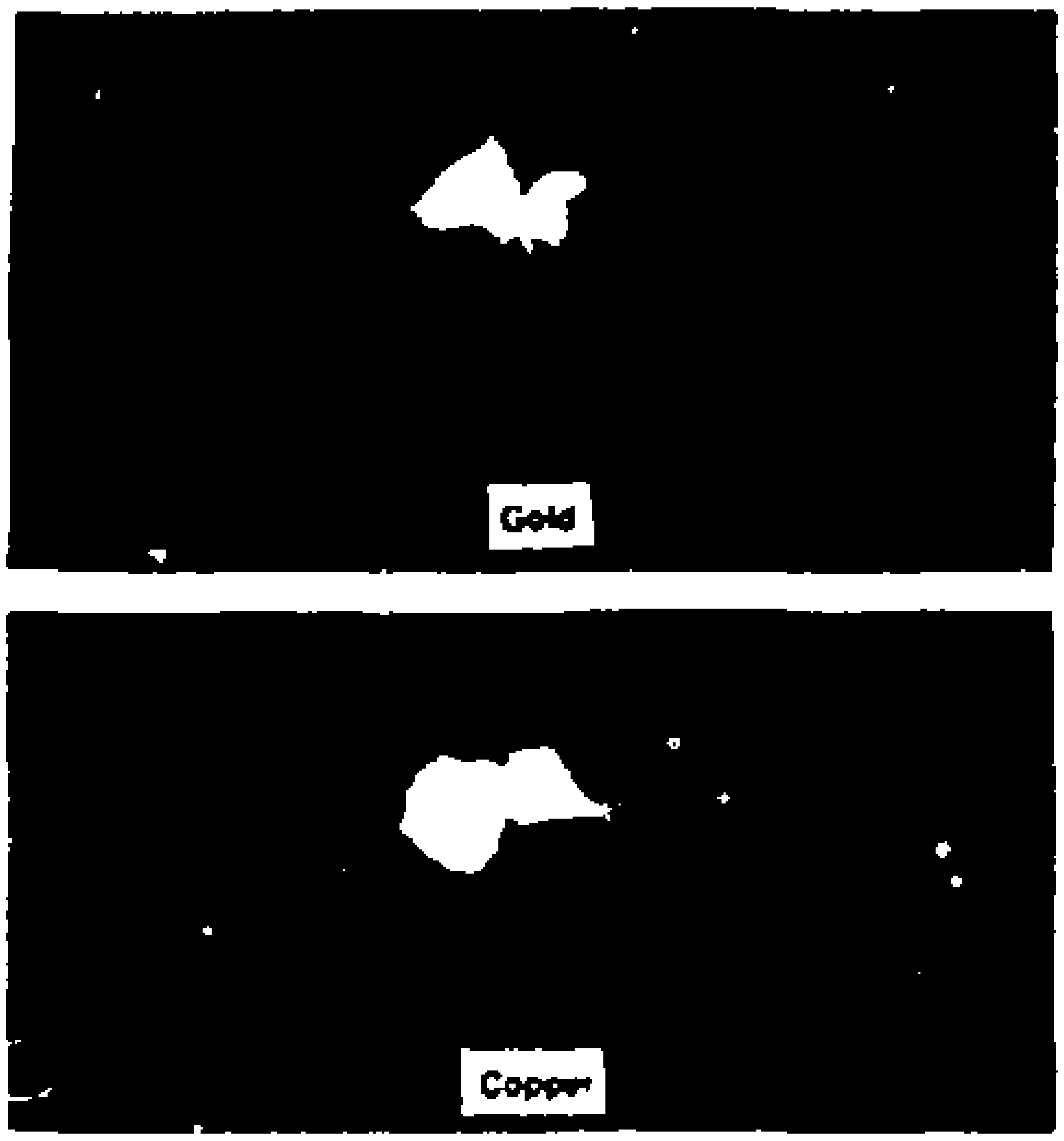

Fig. 4 Luminous arcs occurred at 0.45 V between gold electrodes and at 0.46 V between copper electrodes prior to firm contact closure.

Asperity Dynamics

The events that occur between first asperity contact and arc formation were not all immediately obvious. The initial drop in potential after initial contact can be interpreted as contact and melting of the asperity. The slow rise is probably caused by necking down of the molten asperity by electromagnetic forces, and the arcing could be caused by *an inductively generated voltage on pinch-off of the molten asperity.*

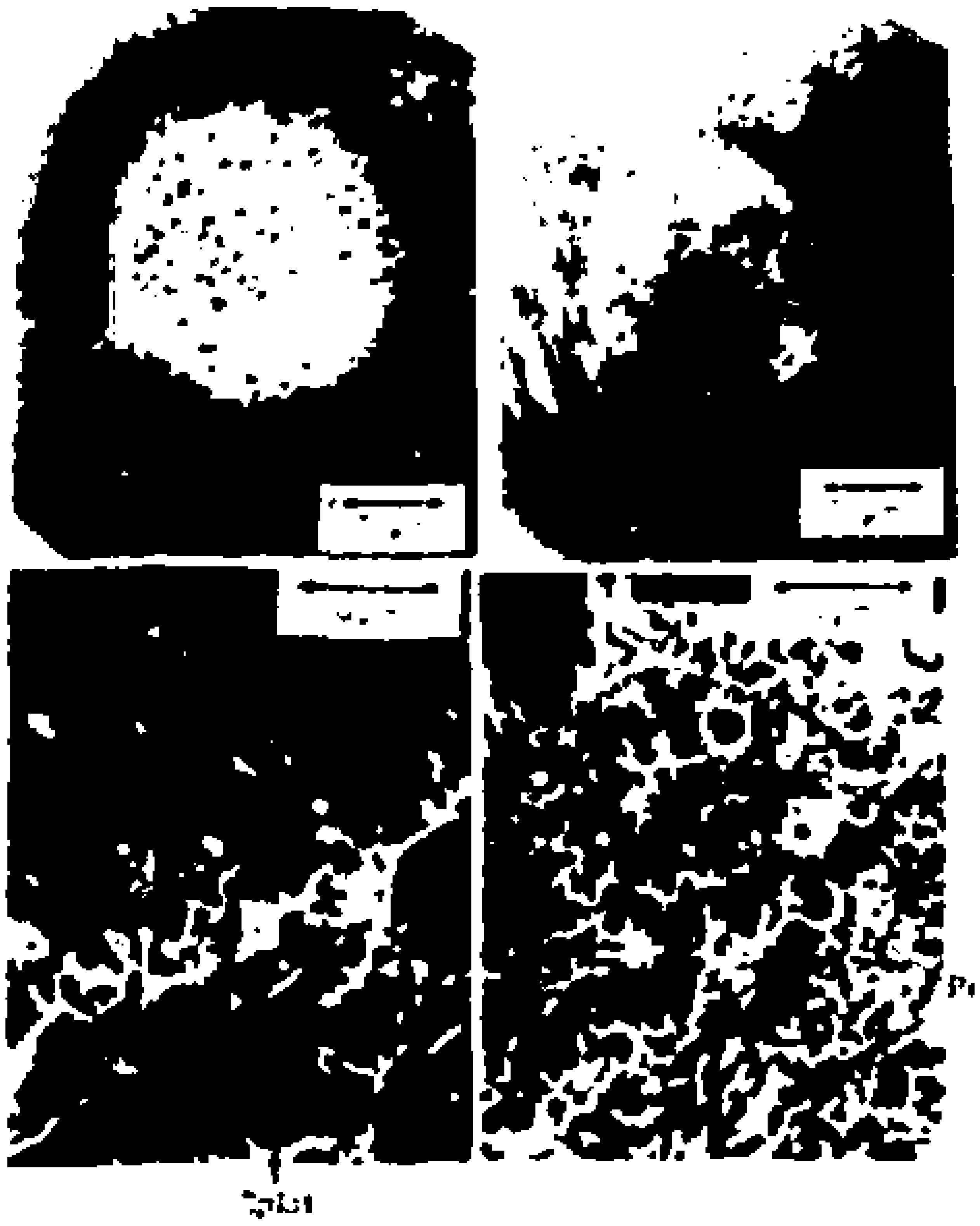

Fig. 5 Gold splats on a gold anode and pits on a gold cathode produced by multiple arcs initiated at open-circuit potentials of 0.45 V. The damage is essentially equivalent for opening and closing contacts without bounce.

TABLE I

Melting, Boiling, and Minimum Arc Initiation Voltages for Electrical Contact Materials (V)

Material	Melting Voltage	Boiling Voltage	Minimum Arc Initiation Voltage*
Ag	0.37	0.76	0.40
Al	0.3		0.40
Au	0.43	0.9	0.45
Cu	0.43	0.8	0.46
Fe	0.8		0.65
Mo	0.75	1.1	0.76
Ni	0.65		0.68
Pt	0.71	1.3	0.75
W	1.1	2.1	1.1

---

*This study.

In the experiments, the size of the asperities involved in arcing ranged from 0.15 to 1.5 μm, based upon microscopic measurement as well as upon the range in times between initial and firm contact closure and the closure rate of 50 μm/s. Asperity size and current were used to calculate magnetic pinch forces. Comparison of the pinch force with surface tension forces which oppose pinch-off indicated that pinch-off is possible for asperity diameters of about 1 μm or less in gold.

The belief that arcing before firm contact closure was initiated by contact and vaporization of asperities was also substantiated by experiments with the extremely smooth gold contacts, in which no arcing prior to closure was observed.

Conclusions

Low voltage, high current, sustained, luminous arcs were found to precede firm contacting of electrical contacts that closed without bounce. Simultaneous oscilloscope traces of the potential and the current during these closures were interpreted in terms of contacting of asperities followed by melting, magnetic pinch-off of the molten metal bridge, and the inductive generation of the arcing voltage. The melting voltages of the contact metals were found to be the lower limits for the initiation of this process. Arcs were not observed on the closure of exceptionally smooth gold contacts. Arc damage to closing contact surfaces is similar to that observed on opening contacts, and could present a serious complication in component testing.

Development of Materials for Hydrogen Storage and Transport

Thermo-mechanical processing or slight modification of chemical composition can improve the ability of steels to resist failure in hydrogen environments.

J. A. Brooks, A. J. West

Introduction

Catastrophic failures resulting from hydrogen embrittlement of engineering materials have occurred in systems ranging from pipelines and machinery to spacecraft fuel tanks. In general, these failures have been the result of inadequate design or improper material selection for the hydrogen service environment.

The use of hydrogen as a future energy source for vehicles and residential and industrial applications will require materials that are relatively insensitive to that element. For both personnel safety and economical system performance, a designer of hydrogen storage tanks (pressure vessels) and hydrogen transport systems (pipelines) needs to understand the limits of specific materials for these kinds of hydrogen service. From the financial viewpoint, a successful "hydrogen economy" will depend on the use of existing natural gas pipelines as well as inexpensive alloys for the construction of new storage tanks and pipelines. From the technical viewpoint, the understanding of embrittling mechanisms in hydrogen will facilitate the development of those inexpensive alloys.

Hydrogen Embrittlement

When materials are subjected to loads in the presence of hydrogen, performance can range from catastrophic failure to no degradation, the degree of embrittlement usually increasing with pressure, time of hydrogen exposure, and the stress to which the components are subjected.

The behavior of alloys exposed to hydrogen can take four forms:

1. No degradation – no effect on mechanical properties
2. Ductility reduction – slight losses in both elongation and fracture ductility
3. Lattice degradation – signified by a failure mode change to cleavage or intergranular fracture
4. Hydride formation – degradation of properties caused by the formation of a brittle second phase

Although aluminum alloys appear to be the only alloys which exhibit no degradation in gaseous hydrogen, other problems such as stress corrosion and limited toughness at high strength levels usually prevent their use. Since these alloys and alloys in category 4 (where hydride formation occurs) are unacceptable for hydrogen storage systems, we will emphasize here the alloys which exhibit ductility reductions in hydrogen (category 2) and discuss only briefly steels that exhibit lattice degradation (category 3).

Austenitic stainless steels (category 2) are the subject of most of our research and development efforts because of their desirable mechanical and corrosion properties and their mild sensitivity to hydrogen environments. Our approach has been to identify materials within this category which have as little ductility loss in hydrogen as possible. However, the techniques used and the knowledge gained from these studies are currently being applied on alloys originally of the third category in an attempt to develop these lower-cost alloys for use in hydrogen systems.

While a thorough understanding of hydrogen embrittlement is not available, research has provided some knowledge of how chemistry, metallurgical structure, and thermomechanical processing can affect hydrogen compatibility.

Factors Affecting Ductility in Hydrogen

We believe that loss in ductility of austenitic stainless steel alloys is caused by interaction of hydrogen with dislocations during deformation. As hydrogen-carrying dislocations encounter small particles or inclusions, such as are normally present in commercial materials, they may tangle or pile up against the particles or inclusions. When this happens a *high* local hydrogen content, well in excess of the equilibrium content, is developed. There is evidence that this local hydrogen, trapped at the inclusions, could reduce the interface strength, form small voids at particles, *and aid void growth by internal pressure.* All these effects aid or accelerate the process of failure. It is of particular significance that changes in void size that have been measured in samples tested in hydrogen can be related to ductility losses.

The deformation mode of a particular alloy can also affect sensitivity to hydrogen. In alloys where dislocations are able to move around particles by a cross-slip mechanism, the dislocations distribute *the hydrogen rather uniformly* throughout the lattice. On the other hand, dislocations which are unable to cross-slip easily, tend to pile up against the particles or boundaries and deposit hydrogen at that local site. This dislocation motion under stress can often be related to stacking fault energy (SFE). A general trend toward increased sensitivity to hydrogen with lower SFE has been observed in many alloy systems. Alloys that cross-slip easily have a high SFE while those exhibiting planar slip usually have a low SFE.

The microstructure of an alloy has also been found to be a sensitive variable in hydrogen embrittlement. A fine grain *size improves strength and toughness as well as resistance to* hydrogen embrittlement. Grain orientation in the microstructure also influences hydrogen resistance, with random orientation usually improving resistance. The presence of brittle second phases such as martensite and delta ferrite can cause increased sensitivity to hydrogen. Microstructural changes can result directly from forming or thermomechanical processing. For example, the effect of high-energy-rate-forging (HERF), which provides a high dislocation-density, fine-grained microstructure, significantly improves the properties of several austenitic stainless steels.

Slight chemistry variations can have a significant effect on hydrogen performance. Not only can these variations affect the formation of second phases such as martensite and delta ferrite, but they can also affect the deformation characteristics. For example, the tensile ductility losses are much greater in 304L than 309 [60% vs. 10% measured reduction in area (RA)] when these alloys are tested in high-pressure hydrogen. We feel that the higher nickel concentration in 309 increases the stacking fault energy, promotes cross-slip, and thus decreases high localized concentrations of hydrogen at dislocation pile-ups as discussed above. Similarly, chromium in concentrations up to 18% has been observed to improve hydrogen resistance. Manganese in concentrations greater than 3% has been found to be deleterious in austenitic stainless steels used to contain *gaseous hydrogen, whereas silicon appears to improve resistance* to hydrogen cracking. Thus changes in alloy chemistry can have large effects on hydrogen susceptibility, and should be considered when additives are planned to improve the toughness or tensile characteristics of a given alloy.

Accelerated Testing for Hydrogen Embrittlement

At room temperature the accumulation of hydrogen in the lattice can be slow. However, high hydrogen concentrations resulting from long-term exposure can be created more quickly by using a thermal-charging technique: exposure to high-pressure hydrogen at elevated temperature. This technique produces the hydrogen concentration profiles that could be expected in a hydrogen storage vessel or pipeline after years of service, and allows us to study in a timely manner the effect of internal (inter-lattice) hydrogen on mechanical properties. Thermally charged and uncharged specimens are tensile tested in high-pressure hydrogen to evaluate the effect of both "internal" and "*environmental*" *hydrogen. A sensitive indicator of ductility losses in hydrogen* is the reduction in area (RA) at the point of fracture. More severely embrittled alloys exhibit changes in fracture mode as well as large RA losses when tested in hydrogen.

Austenitic Stainless Steels – Austenitic stainless steel alloys usually exhibit only minor degradation in ductility when subjected to hydrogen. However, because of their high cost, these alloys are usually used only for very severe environmental conditions, such as highly stressed parts exposed to high-pressure hydrogen, or where a failure cannot be tolerated. The most familiar material of this kind is 304L. Results of experiments to determine effects of in*ternal and environmental hydrogen on the tensile ductility* of 304L are shown in Fig. 1. The RA of annealed 304L was lowered almost 60% by both external hydrogen (at 69

MPa pressure) and internal hydrogen (charged to simulate a reasonable service condition of hydrogen storage at 69 MPa for 10 years). High energy rate forming decreased the sensitivity of 304L to hydrogen. Not only did the HERF *process increase yield strength from 207 to 415 MPa*, but ductility losses in hydrogen were reduced from 60% to only 15%.

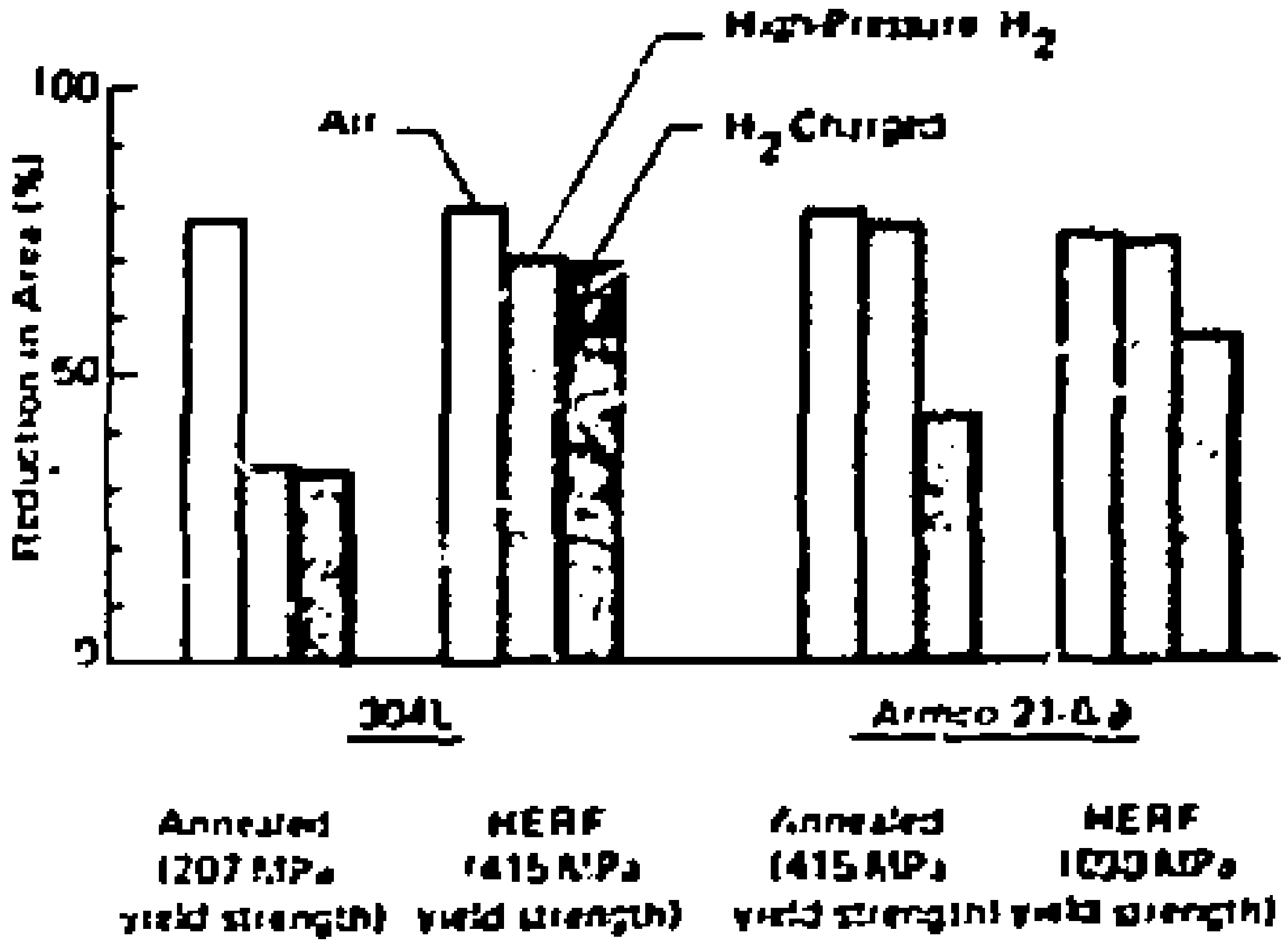

Fig. 1 Ductility of 304L and 21-6-9 stainless steel specimens tested in air, in 69 MPa hydrogen, or after hydrogen-charging, depends upon thermo-mechanical history, for example, high-energy-rate-forging.

One disadvantage of materials strengthened by mechanical *deformation is that the microstructure responsible for im*proved properties can be destroyed during welding. A weld region has properties approaching those of annealed materials. Since welding is usually needed in construction of hydrogen containment systems, weldment performance in the adverse environment is of paramount importance to the successful operation of the system. Welding research, then, *assumes a large role in our alloy development program.*

Weld fillers for 304L typically contain from 2 to 10 vol % of a second phase, the δ ferrite, to reduce the tendency for hot cracking. We have found that welds in 304L exhibit ductility losses in the presence of external but not internal hydrogen. As shown in Fig. 2, fracture occurs along the δ ferrite network resulting in a quasi-cleavage-appearing fracture compared to a completely ductile dimple fracture in samples tested in air. These results suggest that the quantity of ferrite should be limited (2 to 5 vol %) to prevent weld cracking, while minimizing hydrogen embrittlement in 304 welds.

New Stainless Steel Alloys The search for higher-strength materials has led to the use of newer nitrogen-strengthened commercial alloys (21-6-9 and 22-13-5) and a precipitation-hardened alloy we developed specifically for this need (JBK-75). The compositions of these stainless steel alloys are shown in Table I. The nitrogen-strengthened stainless steel alloys have been thoroughly investigated and qualified for use in hydrogen environments. As shown in Fig. 1, the strength of 21-6-9 in the annealed condition, 415 MPa, (about twice that of 304L) is unaffected by external hydrogen. Annealed 21-6-9 exhibits about 45% loss *in RA due to internal hydrogen, whereas only a 20% loss* in RA is observed in the HERFed condition where a yield *strength of ~690 MPa can be achieved.* 22-13-5 exhibits little ductility loss due to either internal or external hydrogen, and can be HERFed to 1035 MPa yield strength.

TABLE I

Typical Composition of Stainless Steel Alloys
(mass %)

Alloy	Ni	Cr	Mn	Si	C	N	Ti	Al	Mo	V	B	Fe
304L	10	19	1.5	0.5	0.02	-	-	-	-		-	Bal
309	14	23	1.6	0.5	0.06	-	-	-	-	-	-	Bal
21-6-9	6	21	9.0	0.5	0.04	0.3	-	-	-	-	-	Bal
22-13-5	13	22	5.0	0.5	0.04	0.3	-	-	2.25	0.2	-	Bal
Commercial A-286	25	15	1.5	0.5	0.06	-	2.1	0.15	1.25	0.25	0.005	Bal
JBK-75*	30	15	Min	Min	0.03	-	2.2	0.2	1.25	0.25	Min	Bal

---

*Developed for weldability and hydrogen compatibility, U. S. Patent 3,895,939

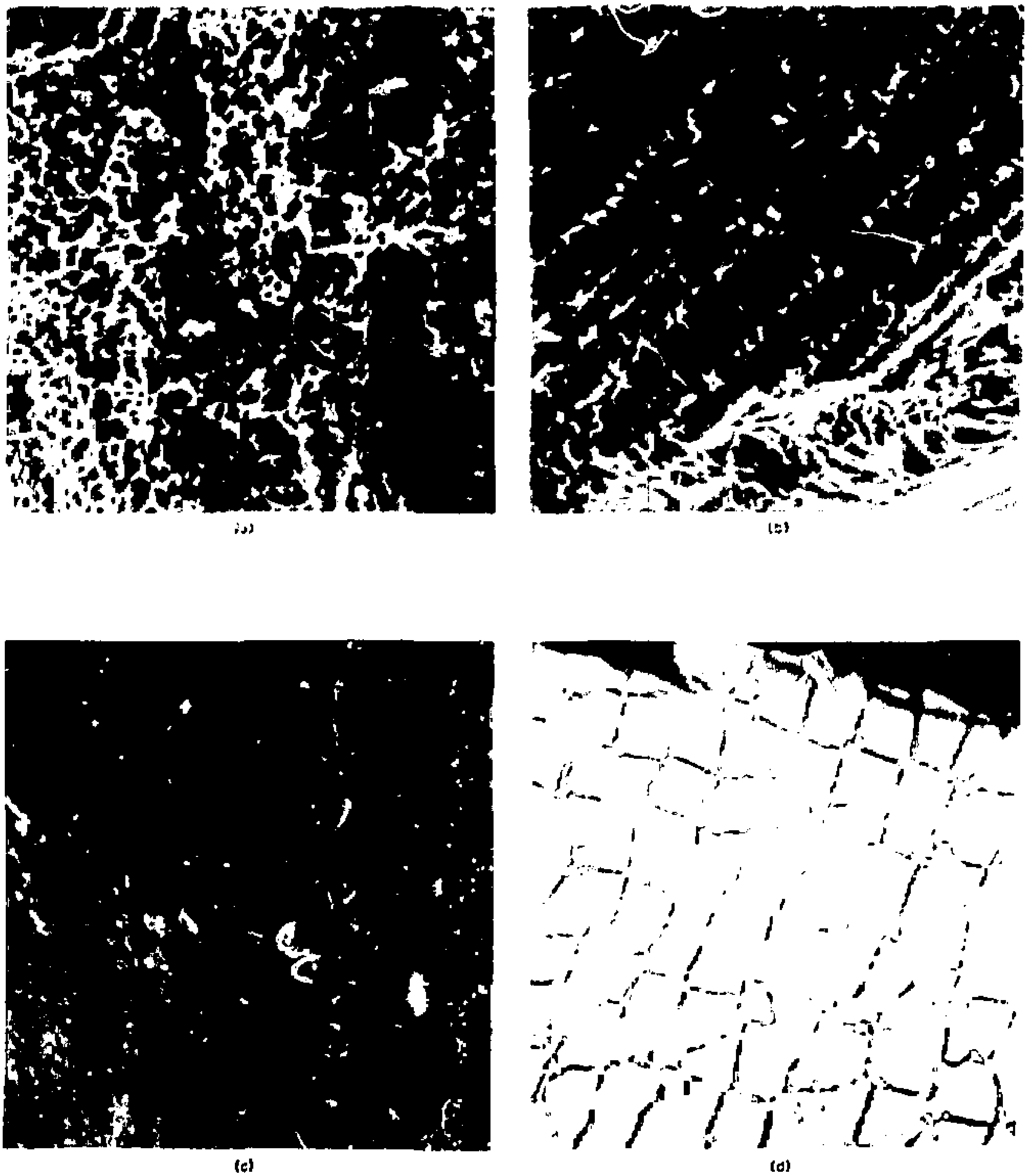

Fig. 2 Microstructure adjacent to fracture surface in 304L with 308 filler weld; appears different in tests uncharged in air (a), and thermally-charged with H_2 at 69 MPa (b); (c) and (d) show microstructure in planes perpendicular to fracture.

The decreased ductility loss of 21-6-9 and 22-13-5 over that of 304L in hydrogen can be attributed to the deformation process. These two alloys have a significantly higher stacking fault energy (SFE) than 304L. In general, the resistance of stainless steels to hydrogen increases with increasing SFE. *This is consistent with the fact that dislocations in alloys having high SFE such as 309, 316, and 22-13-5, are able to move around particles by a cross-slip mechanism and* thereby distribute the hydrogen more uniformly throughout the lattice. On the other hand, dislocations in lower SFE alloys, such as 304L, are unable to cross-slip easily, pile up at particles, and deposit the hydrogen at these local sites. This sequence results in more hydrogen-assisted void growth and lower RA values in the low SFE alloys.

In HERF 22-13-5, welds exhibit a yield strength approaching that of annealed plate (483 MPa) compared with 1035 MPa in the parent material. This strength degradation in the weld often limits the usefulness of the higher strength matrix in an engineering design. In an attempt to attain high strength levels in both the parent material and welds, precipitation-strengthened stainless steel alloys were evaluated. However, we found that these commercial alloys exhibited either poor weldability, poor hydrogen compatibility, or both. *Therefore, an extensive program was initiated to develop an alloy which is readily weldable,* compatible with hydrogen, and exhibits strength superior to the nitrogen-strengthened alloys in the welded and annealed conditions.

Alloys based on commercial A-286, which derives its high strength by precipitation of a small (≈10 nm) coherent phase, $\gamma'(Ni_3[TiAl])$, were studied. *After an earlier investigation showed that small chemistry modifications* could significantly improve weldability, we conducted similar studies to improve hydrogen compatibility. When thermally charged with hydrogen, commercial A-286 exhibits a 50% loss in RA, and the loss is accompanied by a change in fracture mode from ductile rupture to partial intergranular failure. This is of particular concern since fracture mode changes often indicate susceptibility to delayed brittle failure *in service.*

The effect of slight alloy modifications on the strength and RA loss is shown in Table II. Increased Ni content and decreased Mn level reduced ductility losses, while increases in Ti, Al, and Mo increased ductility losses. Even though Ti and especially Mo are potent strengtheners, they must be used in moderation to maintain hydrogen compatibility. The effect of alloying elements on the compatibility can be partially explained by the minor phases formed during the aging-precipitation process. Increases in Ti and Al resulted in an excessive amount of cellular η (over-aged γ', Ni_3Ti) at the austenite grain boundaries. Increasing the Mo level resulted in formation of the χ phase, $Mo_5Cr_6Fe_{18}$. These *phases or interfaces appeared to be embrittled by hydrogen, resulting then in a large amount of grain boundary failure in hydrogen.* However, the formation of second phases other than η cannot explain the effects of elements such as Mn and Ni. Using a rationale based upon dislocation motion and interactions with the γ' precipitate, the behavior of Mn and Ni can be explained. In alloys containing *an ordered, coherent γ' precipitate, slip is initially* planar because dislocations tend to cut or shear γ' particles and thereby enforce continued slip along the first planes *which are active. This appears to be the case for A-286 and results in the transport of hydrogen to the sensitive grain* boundary region where partial intergranular failure occurs.

TABLE II

Tensile Properties – A-286 Type Alloys

Description	Yield Strength (0.2% strain) (MPa)	Ultimate Tensile Strength (MPa)	RA (%)	% RA Loss From Charging
*Commercial A-286**				
(low C ~0.03)	795	1100	35	48
Very low C	779	1105	[illegible]	40
Low C, B	760	1160	48	46
Low C, Si, B	760	1180	44	61
Low C, Mn, Si, B	740	1190	50	14
Low C, 35% Ni	760	1160	48	21
Low C, Mn, Si, B,				
*30% Ni***	760	1305	65	11
Low C, Mn, Si, B,				
20% Ni	705	1035	51	27
Low C, Mn, Si, B,				
1% Al	675	1100	52	38
Low C, Mn, Si, B,				
2.6% Ti	730	1330	47	21
Low C, Mn, Si, B,				
2.6% Ti, 6% Mo	1055	1375	23	78

---

*Composition shown in Table I.

**Shown as JBK-75 in Table I.

NOTE: 1200 K 2 hours, water quenched, aged 16 hours 990 K.

Conversely, it has been shown that incoherent precipitates can act as traps for hydrogen as hydrogen-carrying dislocations tangle about the precipitate. For example, a fine dispersion of 2% ThO_2 in Ni can confer hydrogen compatibility on this material which is otherwise severely embrittled by hydrogen transported to the sensitive grain boundaries.

Particles such as γ' in A-286 will become incoherent (a crystallographic interface forms at the precipitate boundary) after a critical amount of strain has occurred. If the strain required to cause coherency loss is small, the particle interfaces can act as hydrogen traps before much hydrogen is transported to the grain boundaries. The larger the lattice parameter mismatch between the matrix and γ' precipitate, the less strain is required to cause coherency loss. This rationale is helpful in explaining why removal of C, C+B, and C+B+Si have essentially no effect on RA losses: these elements have very little effect on lattice parameters. Conversely, the marked effect of Mn removal evidently arises from the rather large effect of Mn on lattice parameters; the three lowest RA loss alloys (Table II) have the lattice parameters they do largely because of Mn removal. Addition of Ni has a weaker effect, but it also reduces lattice parameters and thus increases the lattice mismatch.

Therefore, good strength, weldability, and hydrogen compatibility require that commercial A-286 be modified. By lowering the Mn and increasing the Ni content, only 11% loss in RA occurs due to hydrogen charging, compared to a 50% loss in RA for commercial A-286. In addition, in JBK-75 fracture occurs by completely ductile void nucleation and growth, compared to partial intergranular failure in commercial A-286. This new alloy has an annealed yield strength of 760 MPa and can be HERFed to yield strengths above 1035 MPa.

Development of Compatible Inexpensive Alloys As discussed earlier, the economic feasibility of using hydrogen as a primary energy source depends strongly on the ability to use inexpensive materials to contain and transport hydrogen. For example, constrained by high capital costs, one would not use stainless steels for very large storage vessels or new pipelines. In addition to the large amount of capital tied up in the existing natural gas pipe network, the nearly critical shortages of alloying elements in stainless steel (such as chromium) would prevent the production of sufficient quantities. Consequently, it is imperative that techniques be developed for improving the hydrogen compatibility of inexpensive alloys as well as for clearly defining the operating limits of existing components (pipelines) which will operate in hydrogen. Knowledge of the materials limits in hydrogen service will then define the needs for special protective barriers such as liners or coatings or other reinforcements which will make the component usable

Our discussion thus far has shown how certain processing and chemical composition modifications can improve the hydrogen compatibility of stainless steels. We have seen that the nature of deformation processes directly affects hydrogen sensitivity. It was shown that HERFing improves compatibility by changing the dislocation microstructure, and that microstructural control, such as the addition of a second phase (dispersion or precipitation), influences an alloy's sensitivity to hydrogen. Finally, it was noted that through small chemistry changes it is possible to reduce hydrogen sensitivity. Can these principles be applied to some of the inexpensive alloys susceptible to lattice degradation? Our experience to date is that these principles and others can improve the useful range of low-alloy structural steels for hydrogen service. At worst, we will be able to clearly define the operational limits of such alloys and use these data to ensure proper maintenance and quality control.

Preliminary testing of a 1018 mild steel in the cold worked and HERFed conditions has revealed some interesting facts. As shown in Table III, cold worked 1018 steel (σ_y = 593 MPa) showed a RA decrease from 47% to 31% when tested in high-pressure hydrogen. Note also that the uniform elongation is quite low (~2%) even in air. HERF samples, on the other hand, exhibited slightly lower yield strength

TABLE III

Tensile Properties – 1018 Steel

	Atmosphere	Yield Strength (MPa)	Ultimate Strength (MPa)	RA (%)	Uniform Elongation (%)
Cold Worked	Air	593	622	47.1	2.35
	69 MPa H_2	617	631	31.0	1.80
HERF	Air	551	612	44.6	7.4
	6.9 MPa H_2-He	500	687	34.1	6.4

(551 MPa vs. 593 MPa) with a greater than threefold improvement in uniform elongation. HERF samples that were charged with H_2 and tested 50/50 vol% H_2/He gas mixture showed only a 13% decrease in uniform elongation as compared to the air samples. The data, although sketchy, suggest that beneficial effects in 1018 steel can be derived from thermal-mechanical processing. We are making detailed studies of these effects.

Conclusions

The compatibility of materials in high-pressure hydrogen has been observed to be dependent on deformation characteristics, thermo-mechanical processing, microstructure, chemical composition, and the presence of welds. Using these concepts, we developed a new high-strength austenitic stainless steel alloy for use in hydrogen. A detailed understanding of performance in hydrogen is not yet available to facilitate the design of inexpensive structural materials for large scale hydrogen storage and transmission systems. However, numerous specific observations regarding the influence of the above variables on hydrogen cracking resistance should permit the design of low-cost alloys having minimum sensitivity to hydrogen environments. Thus, improvements of low alloy steels for hydrogen service are possible, and the limits of these steels can be defined to permit safe use of these materials for hydrogen transportation and storage.

Measurement of Thermal Transients

With thermal sensor response models we can improve the accuracy of measurements from transient thermal experiments.

N. R. Keltner

Introduction

Analysis of transient thermal experiments requires accurate knowledge of the temperature and/or heat flux histories at the surfaces of a test item. When experiments involve rapid changes in temperature or heat flux, typical sensors may not indicate the true history, and estimates of measurement errors become important for data analysis. For the data analysis, exponential approximations have generally been used to characterize the transient responses of the sensors. Such approximations can lead to serious errors because the transient response is usually not exponential; actual transient response is not indicated by sensor calibration because calibrations are at steady-state or quasi-steady-state conditions.

To make an accurate interpretation of data from transient thermal experiments, one must understand thoroughly the transient response characteristics of the sensor installation. In many cases, the response characteristics depend not only upon the sensor itself but also upon the specific substrate material and the manner of mounting. The development of thermal sensor response models has allowed us to determine data corrections accurately, and thus to determine accurate thermal histories in high-heat-flux test environments.

Response Models

We have studied thermal sensor response in conjunction with several experimental programs at our radiant heat facility and have used experimental, analytical, and numerical techniques to develop response models for the following:

- Foil thermocouples (attached to the surface by flame-sprayed aluminum oxide).
- Intrinsic thermocouples (the thermoelectric circuit includes the material on which the measurement is made).
- Circular-foil heat-flux gages (a radial temperature gradient, which is proportional to flux, is measured by a differential thermocouple between the foil center and a circumferential heat sink).
- Strain gages and platinum resistance thermometers (attached by flame-spray process).

By experiment we have established response models for all of these sensors, measuring response to known step or ramp inputs. By using measured responses and mathematical theory (e.g., Duhamel's convolution theorem for linear systems), we could estimate response for an arbitrary input. For some of the sensors it was also possible to construct analytical or numerical models for the response to either step or ramp inputs. Close agreements between the predictions of the analytical, numerical, and empirical models support their validity.

For both foil and intrinsic thermocouples, we used this experimental procedure for determining the step response model:

- The thermocouple was attached to the material sample. (For the intrinsic thermocouple, wires were individually attached to the sample.)
- A capacitor bank was discharged through the sample to produce a rapid (less than 50 μs) increase in temperature, and the output of the thermocouple was monitored on oscilloscopes.

- A least-squares analysis of data provided an estimate of the transient response characteristics.

Figure 1 shows results for six foil thermocouples. The spread in the data is caused by slight differences in nominally identical installations. For this sensor installation, we obtained a best estimate of the response and bounds on the fastest and slowest response. When these responses are compared with an exponential curve, we see that the assumption of exponential response would give inaccurate results if used to analyze transient data.

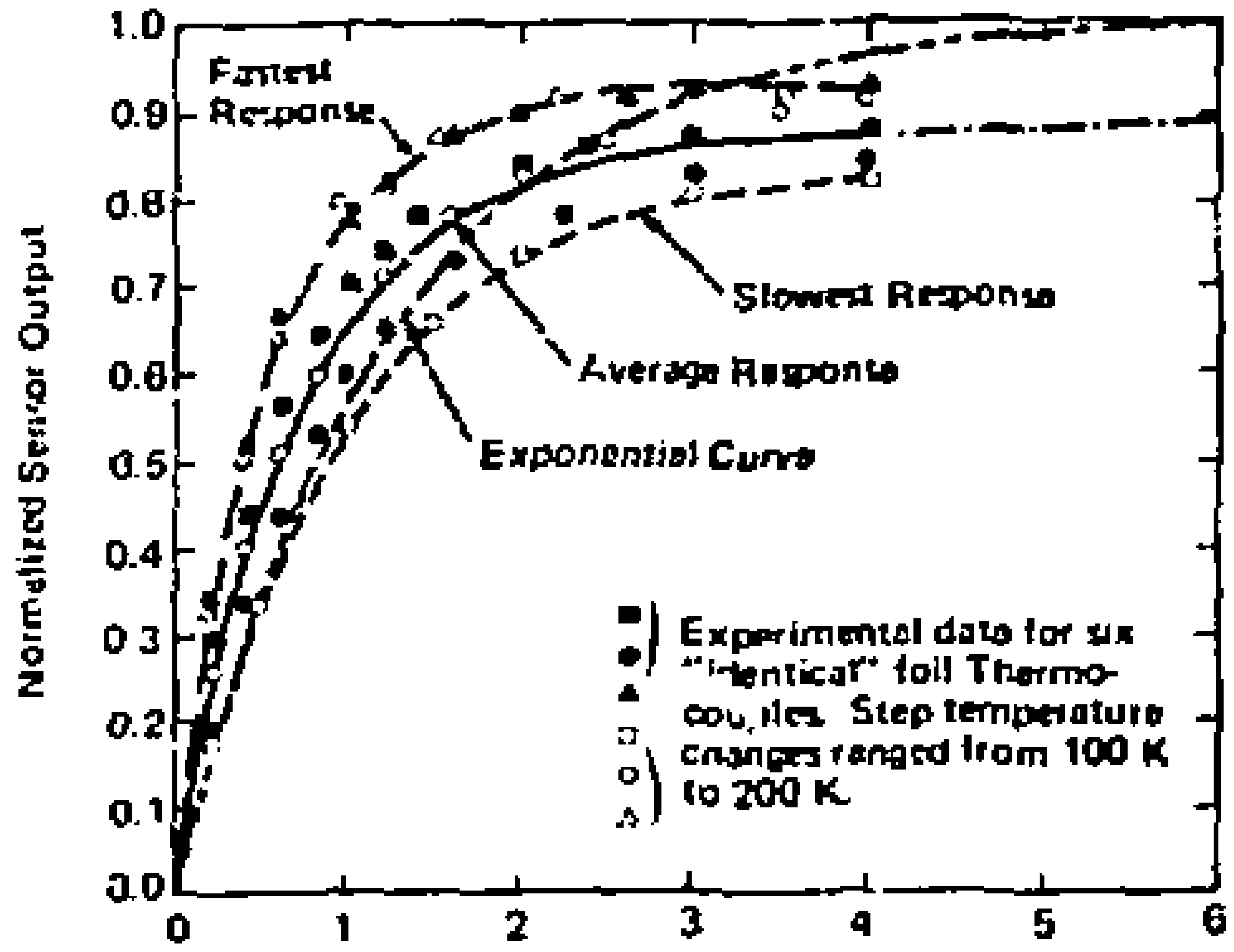

Fig. 1 *Comparison of an exponential curve with transient responses of foil thermocouple installations on a carbon composite material shows that the responses cannot be accurately approximated by a simple exponential.*

For the intrinsic thermocouple, we obtained an analytical step response model with a technique called quasi-coupling. This technique was developed to solve transient problems with an interface between two geometrically distinct regions, each of which can be analyzed separately by using appropriate coordinate systems. We developed expressions for the response of each wire (modeled in Cartesian coordinates) and the substrate (modeled in oblate spheroidal coordinates) to a step change in temperature at the interface. With these expressions we obtained an explicit expression for the interface temperature in terms of a set of eight equations. These equations are used to determine step response in a successive matching procedure for temperature and total integrated heat flow across the interface region.

We found good agreement between the analytical response model and a finite difference numerical model for the intrinsic thermocouple. In Fig. 2 predictions of the analytical model are compared with the experimental data used for the empirical model for one installation. When we examined the response of various intrinsic thermocouple installations we noted that the substrate greatly affected response. (For one type of thermocouple wire, the time to 95% response to a step temperature change varied by a factor of 330, depending upon the type of substrate material.)

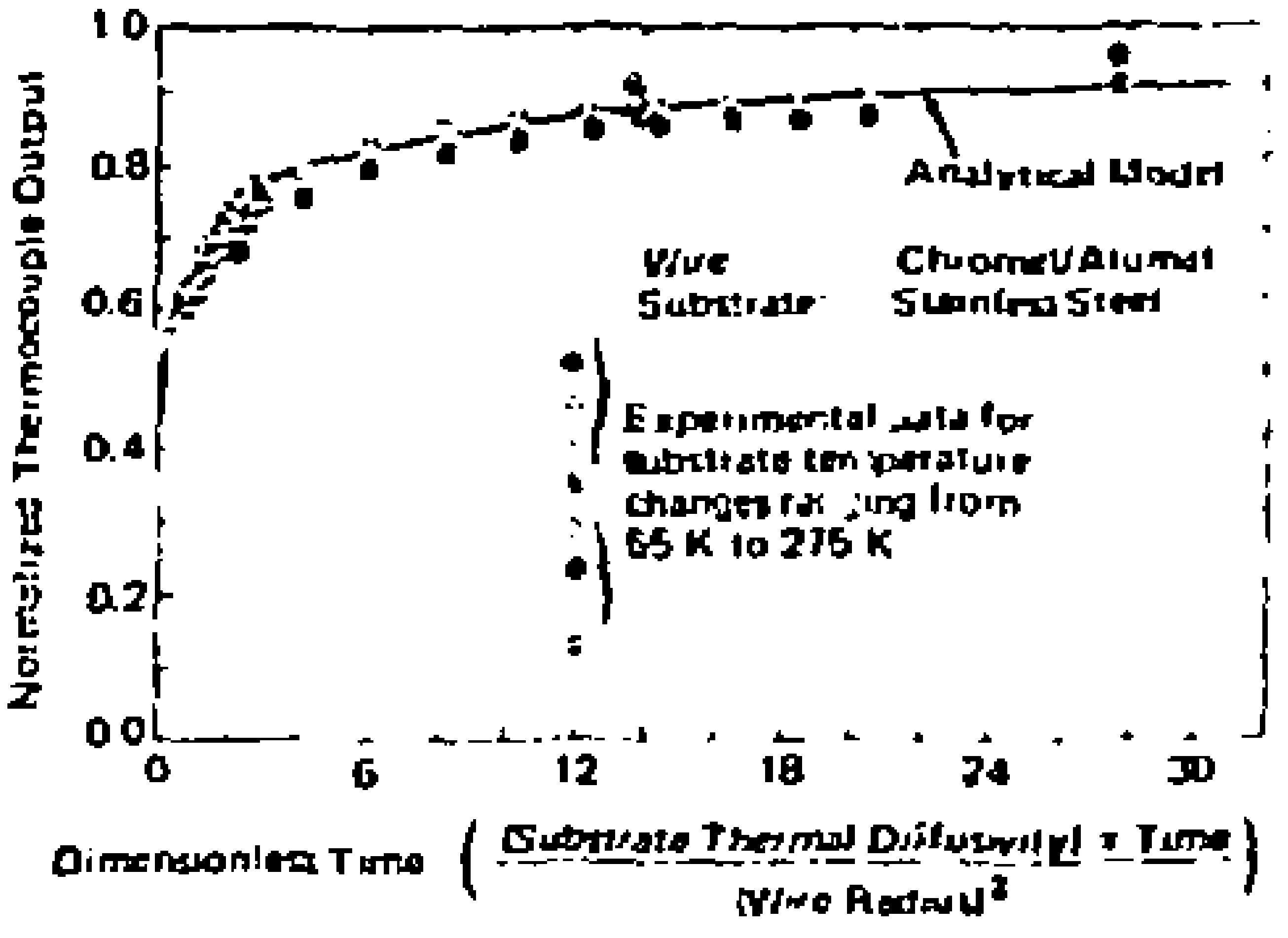

Fig. 2 A comparison of the output of an intrinsic thermocouple predicted by an analytical response model with experimental data shows good agreement.

The quasi-coupled solution technique was also used to develop an analytical response model for the circular-foil heat-flux gage. Figure 3 compares predictions from this analytical model with experimental data obtained by exposing several gages to a step change in incident radiant heat flux.

We have not yet been able to obtain close agreement between empirical and theoretical models for strain gages and resistance thermometers. We have used empirical models successfully and are trying to improve theoretical modeling.

Applications in Thermal Experiments

In a recent series of experiments we subjected cylindrical and conical carbon/carbon material (sometimes used as reentry vehicle heatshields) samples to thermal shock. The samples were rapidly inserted into a cylindrical heater array operating at temperatures as high as 3000 K. We needed accurate values of the absorbed heat flux at the outer surface for thermal stress calculations.

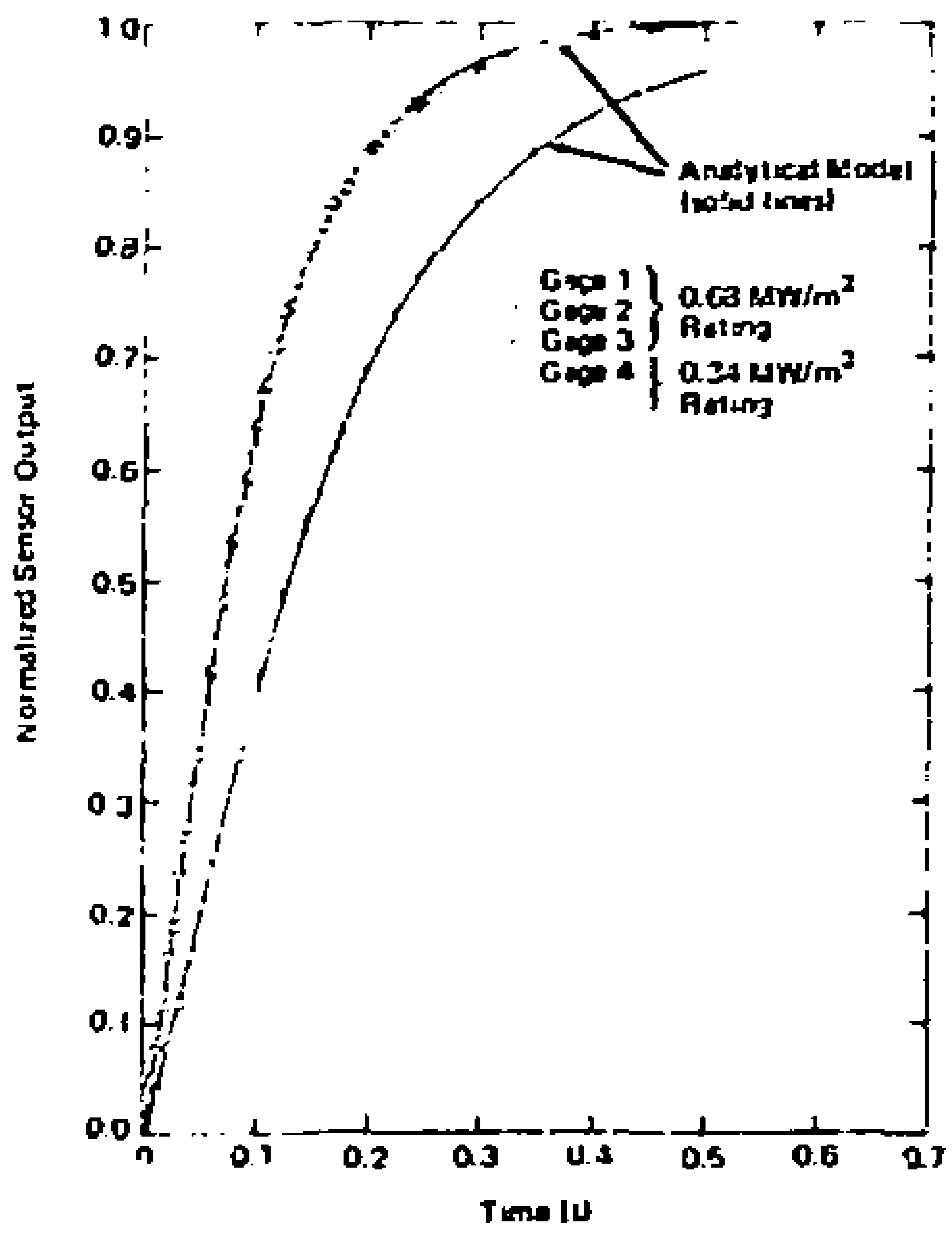

Fig. 3 Circular-foil heat-flux gage outputs predicted by an analytical model agree well with experimental data.

In one method for determining surface flux, we used surface properties, geometrical factors, and data from circular-foil heat-flux gages to calculate absorbed heat flux. In the second method, we used foil thermocouples to measure the inner-surface temperature history. When the absorbed heat flux was calculated from this measurement by assuming that the thermocouples responded exponentially, the heat flux levels were 20% to 40% below the values obtained from the first method. We resolved the discrepancy by using the best estimate of the flux history (from heat flux gage measurements) to calculate the inner surface temperature history and then numerically convoluted that history with the empirically developed thermocouple response model to predict the thermocouple output (Fig. 4).

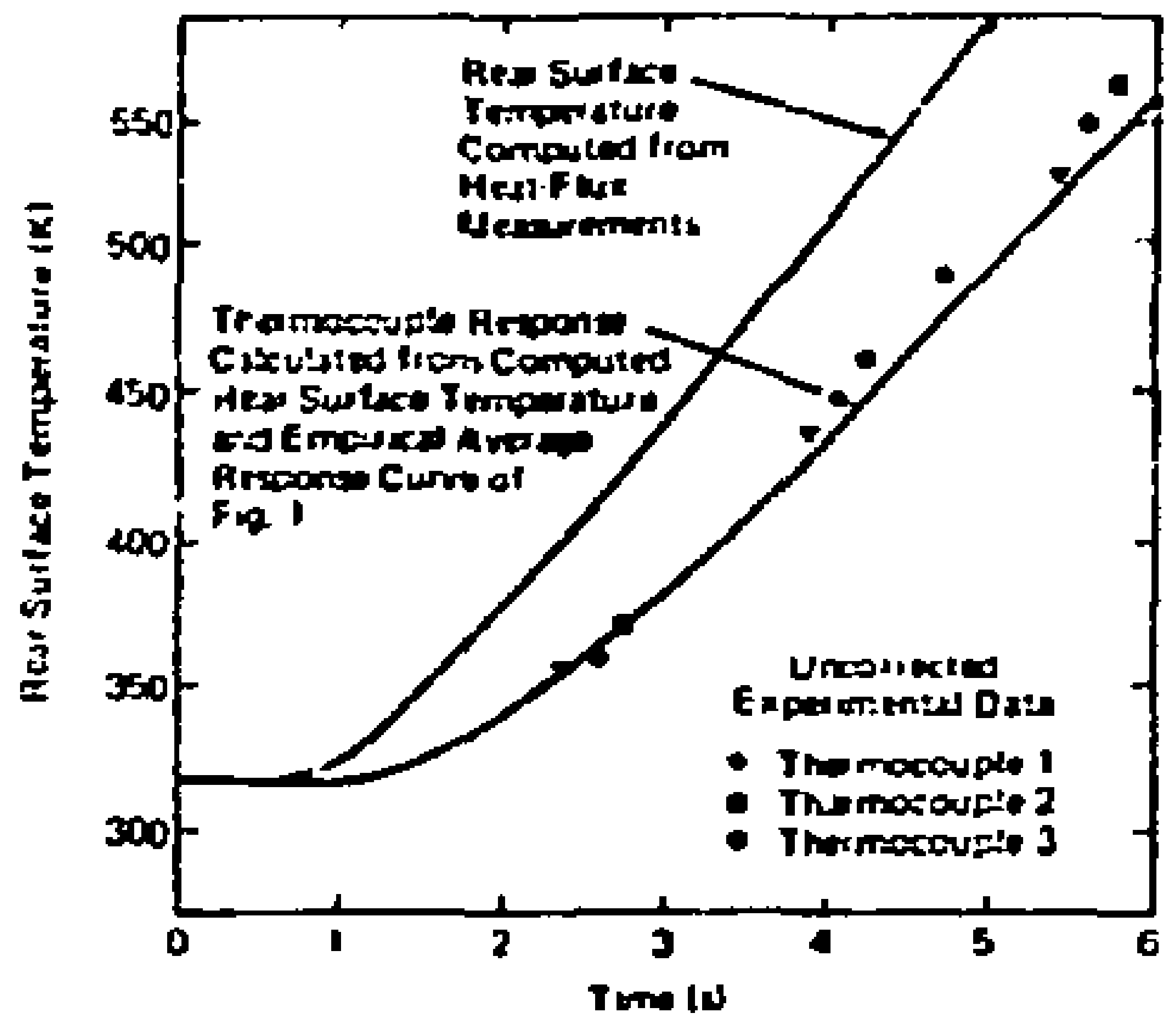

Fig. 4 In a cylindrical radiant heating experiment, rear-surface foil-thermocouples indicated temperatures *were lower than computed from heat-flux measurements.* Use of the empirical response model shown as average response in Fig. 1 gave a corrected thermocouple response that agreed with the thermocouple data.

In another application, we used the intrinsic thermocouple numerical model to analyze a proposed pulsed reactor experiment to determine phase change temperatures and parameters of a uranium alloy. For this experiment, a two-wire intrinsic fission thermocouple (the substrate is a fissionable material) was proposed. Figure 5 reveals the large difference between the substrate temperature and the temperatures at the thermocouple wire attachment points. Because the temperature difference between the two junctions suggests that data reduction will be difficult (a three-element thermoelectric circuit with two unknown junction temperatures), we recommended that the experiment be redesigned.

We have made several other applications of sensor response models:

- To study oscillatory behavior in a heat flux feedback control system, providing offset signals to compensate for thermal inertia and to minimize oscillation.
- To compensate for apparent thermal strain in strain gage measurements when surface temperature is rising at up to 200 K/s.

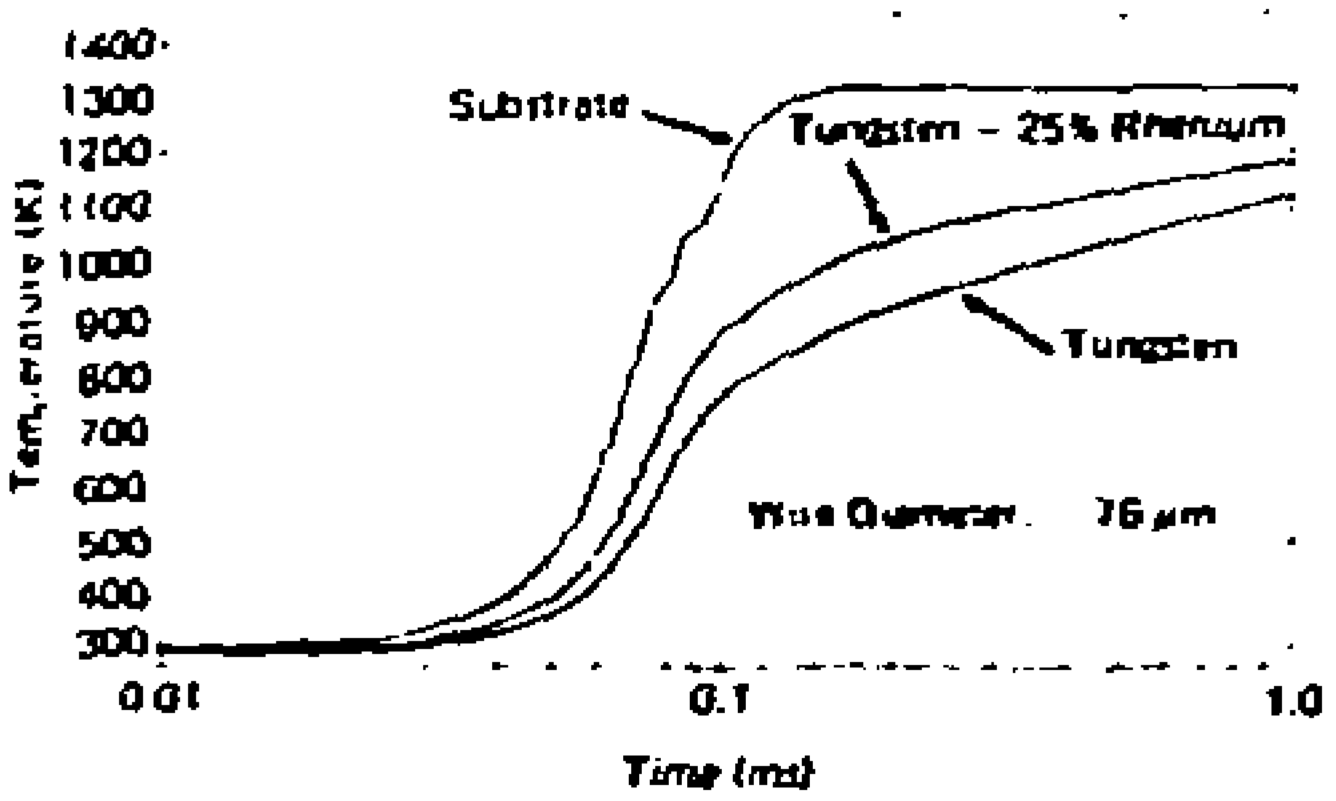

Fig. 5 Numerical response model was used to predict junction temperatures in a two-wire intrinsic thermocouple with a fissionable material substrate, proposed for a reactor experiment. The large temperature difference between the two junctions indicated that the experiment should be redesigned.

- To develop a numerical deconvolution technique for experiments using intrinsic thermocouples over temperature ranges of several hundred kelvins. Step response information and thermocouple data are used to calculate the true surface temperature history

Conclusions

Accurate sensor response models can be used to improve the accuracy of measurements from a transient thermal experiment, and provide accurate estimates of dynamic errors in the data. In many cases error correction formulas or procedures will permit recovery of usable data from otherwise unusable sensor outputs. The models can also be used to select the best sensor for a specific experiment application.

Lithium Niobate Stress Transducers

Determination of piezoelectric characteristics of lithium niobate has led to development of new transducers for measuring fast, high-level stress pulses.

R. A. Graham

Introduction

In the almost one hundred years since the piezoelectric effect was discovered, the phenomenon has been used in a number of devices for a wide range of applications. Although many different crystals generate piezoelectric charges when they are compressed, quartz has been used as the active element in most piezoelectric applications since it has many excellent properties, including reproducible, stable behavior. We have investigated another material, lithium niobate, and found that it is superior to quartz for many piezoelectric stress-transducer applications.

Piezoelectric crystals have orderly three-dimensional structures, which affect the quantity of charge generated at the sample surface when stress is applied in specific directions. For a given direction of stress, the charge generated per unit area by the internal polarization is usually directly proportional to the applied stress or strain. The constant of proportionality, called the piezoelectric constant, depends upon the crystallographic direction in which stress is applied and the direction in which the charge is detected. For example, a piezoelectric crystal could have as many as eighteen piezoelectric constants to define polarization measurements in any of three directions for three different directions of both normal stress and shear stress. Thus the piezoelectric response of a transducer will depend markedly on the direction in which the active element is cut from the crystal.

Common orientations for quartz sample "cuts" (x-cut, y-cut, and z-cut) with respect to the crystal axes are shown in Fig. 1. For lithium niobate, the most useful orientations for stress transducers are z-cut, y-cut, and 36-degree-rotated-y-cut (Fig. 2).

New transducer performance characteristics are possible since lithium niobate has several properties that are significantly different than those of quartz. Lithium niobate has four piezoelectric constants whereas quartz has only two. In addition, lithium niobate exhibits a piezoelectric response to uniform hydrostatic pressure, whereas quartz does not. Furthermore, most piezoelectric constants of lithium niobate are much larger than those of quartz. Lithium niobate gages have the potential for measurements at higher temperature than possible with quartz gages, since quartz goes through a phase transition at 850 K, while

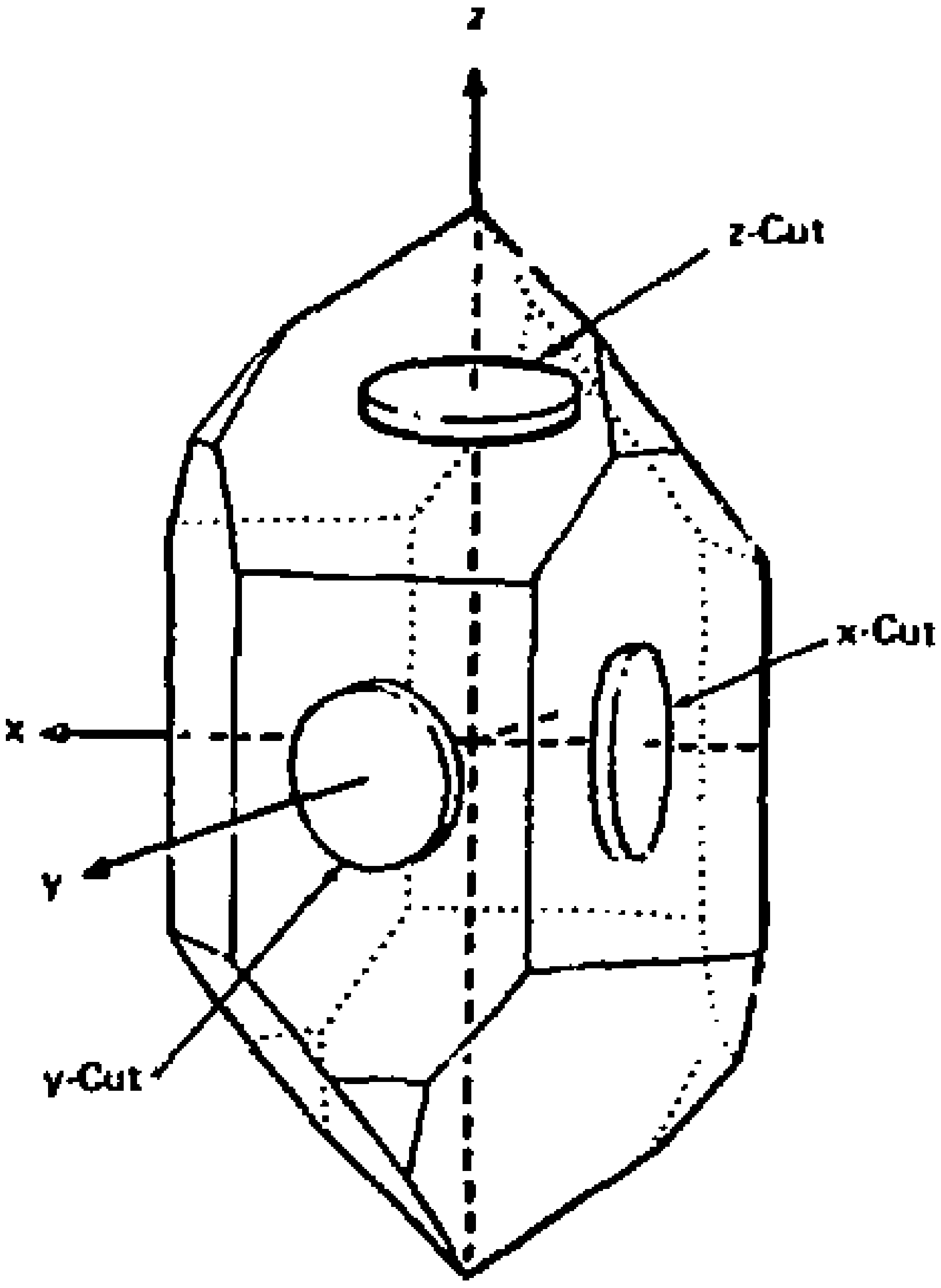

Fig. 1 The properties of samples cut from single crystals depend markedly on the orientation of the sample with respect to the crystal axes. The orientations of common sample cuts are indicated on this sketch of a natural quartz crystal.

lithium niobate remains piezoelectric up to 1500 K. Although there have been problems in the past in growing good single crystals of lithium niobate (the first crystals were grown only about fifteen years ago), it appears that those problems have now been solved.

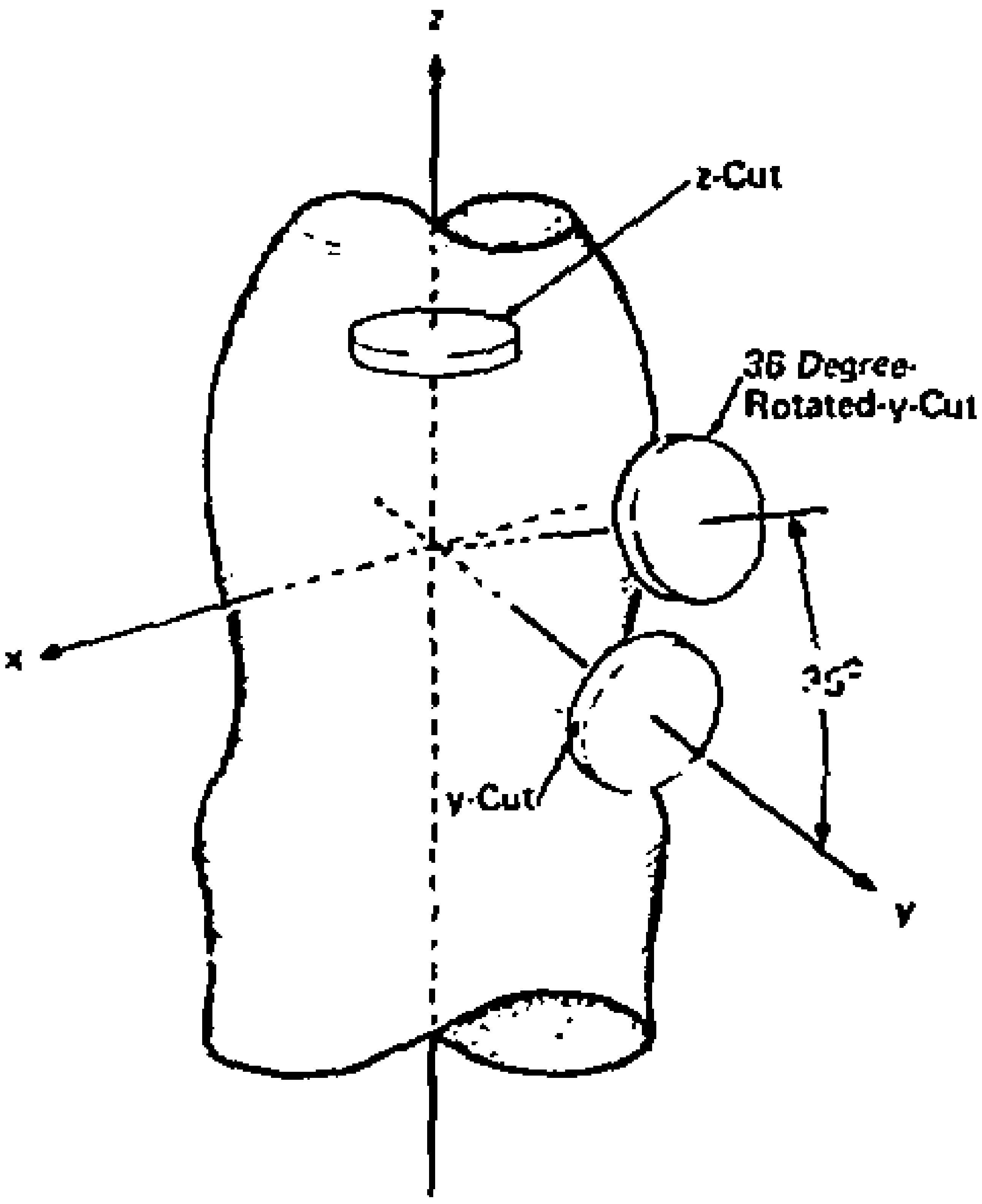

Fig. 2 Single crystals of lithium niobate are grown artificially in the form of boules, typically as large as 50-mm in diameter. Orientations of disks most useful for transducer applications are indicated relative to the crystal axes.

We previously developed an x-cut quartz piezoelectric gage* that could be used for time-resolved stress measurements to 4.0 GPa. This gage has proven especially valuable for materials studies both in the laboratory and in the field. It now appears that with lithium niobate we can develop smaller gages, and also reduce problems associated with signal-to-noise ratios at low stresses. Furthermore, the unique hydrostatic response of lithium niobate provides a new measurement capability.

In this article we will describe an investigation of lithium niobate for measurements of impulsive stress or pressure at levels much higher than required for more conventional piezoelectric applications. First, it is important to consider the special problems posed by the measurement of high pressure impulsive loads with piezoelectric crystals. Studies of the piezoelectric response of lithium niobate to impact loading and to high static pressure will then be described.

Response of Piezoelectrics to Impulsive loads

Piezoelectric gages to measure stress or pressure pulses are used in either of two distinctly different modes, the "current-mode" or the "charge-mode." In both, the active elements are piezoelectric disks; however, their responses provide qualitatively different measurement capabilities, and the responses must be studied by different techniques.

The current-mode is used for measurement of the stress-time characteristics of fast-rising stress pulses. As indicated in Fig. 3 the current-mode requires circuits with short electrical time constants, and gages that are thick relative to the

	Current Mode Gages	Charge-Mode Gages
Rise Time	Typically few ns	Typically hundreds of ns
Pulse Duration or Recording Time	Typically few μs	Typically many ms
Configuration	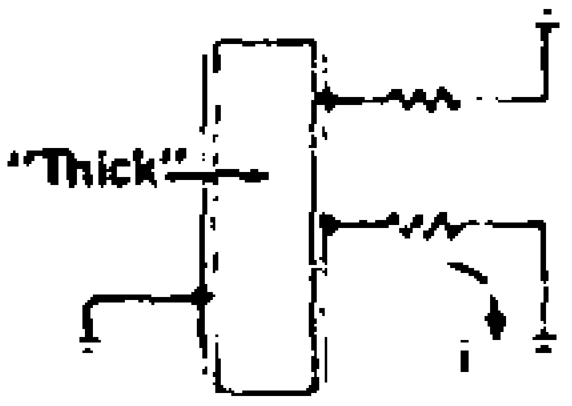	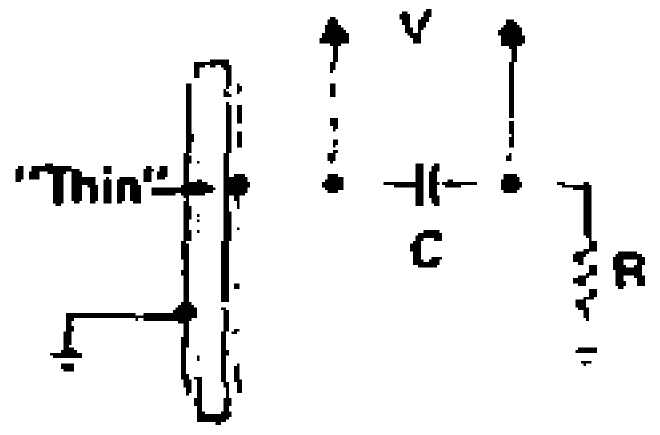
Circuit Time Constant	$RC < 10^{-9}$ s	$RC > 10^{-1}$ s
Output Signal	$i \propto$ Stress	$V \propto$ Stress

Fig. 3 Piezoelectric gages to measure impulsive loads may be constructed in either the current mode or the charge mode. The mode of operation depends upon electrical and mechanical time constants of the gages and circuits which are selected relative to either the risetime or pulse duration of the stress pulse.

---

*U. S. Patent 3,307,052

stress pulse. In this mode the measurable pulse durations are less than the transit times of stress pulses through the gages (typically a few μs).

On the other hand, the charge-mode of operation is used for the measurement of the stress-time characteristics of stress pulses of long duration. As indicated in Fig. 3, the charge-mode requires circuits with long electrical time constants and gages that are thin relative to the widths of the stress pulses. In this mode the measurable rise-times are longer than the transit times of the stress pulses through the gages (typically $\sim 10^{-1}$ μs).

The differences between current-mode and charge-mode gages, summarized in Fig. 3, determine the methods selected for studying the suitability of lithium niobate for transducer applications. The current-mode gage is studied by measuring the piezoelectric response to a direct impact, but the charge-mode gage is studied by measuring the piezoelectric response to quasi-static stresses.

Under the large stresses or pressures resulting from typical impulsive loads, contributions from nonlinear piezoelectric constants may be significant. Since values for nonlinear constants are generally not known, the investigation of piezoelectric crystals for stress transducer applications is necessarily concerned with both linear and nonlinear piezoelectric constants. Furthermore, the large stresses destroy the gage after the desired signals have been recorded. This "one-shot" gage operation prevents direct calibration under typical conditions of use; hence, the reproducibility of material constants provides the basis for confidence in the reproducibility of the gage output signals.

Response of Lithium Niobate to Impact Loading

Current-mode piezoelectric gage systems are used to measure stress profiles produced by impact, explosive loading, pulsed electron-beam irradiation, Q-switched-laser irradiation, or intense pulsed x-ray irradiation. These stress pulses may have complex shapes which change significantly in a few nanoseconds. Properties of lithium niobate for measuring such stress pulses were determined by subjecting disks to carefully controlled impacts at precisely known velocities.

Figure 4 shows a piezoelectric sample mounted at the muzzle of a compressed gas gun. A projectile faced with an impactor material is accelerated to a preselected velocity, and impacted directly upon the sample. Immediately prior to impact, the velocity of the projectile is precisely measured. Upon impact, a shock-wave propagates through the sample, producing a current in the external circuit.

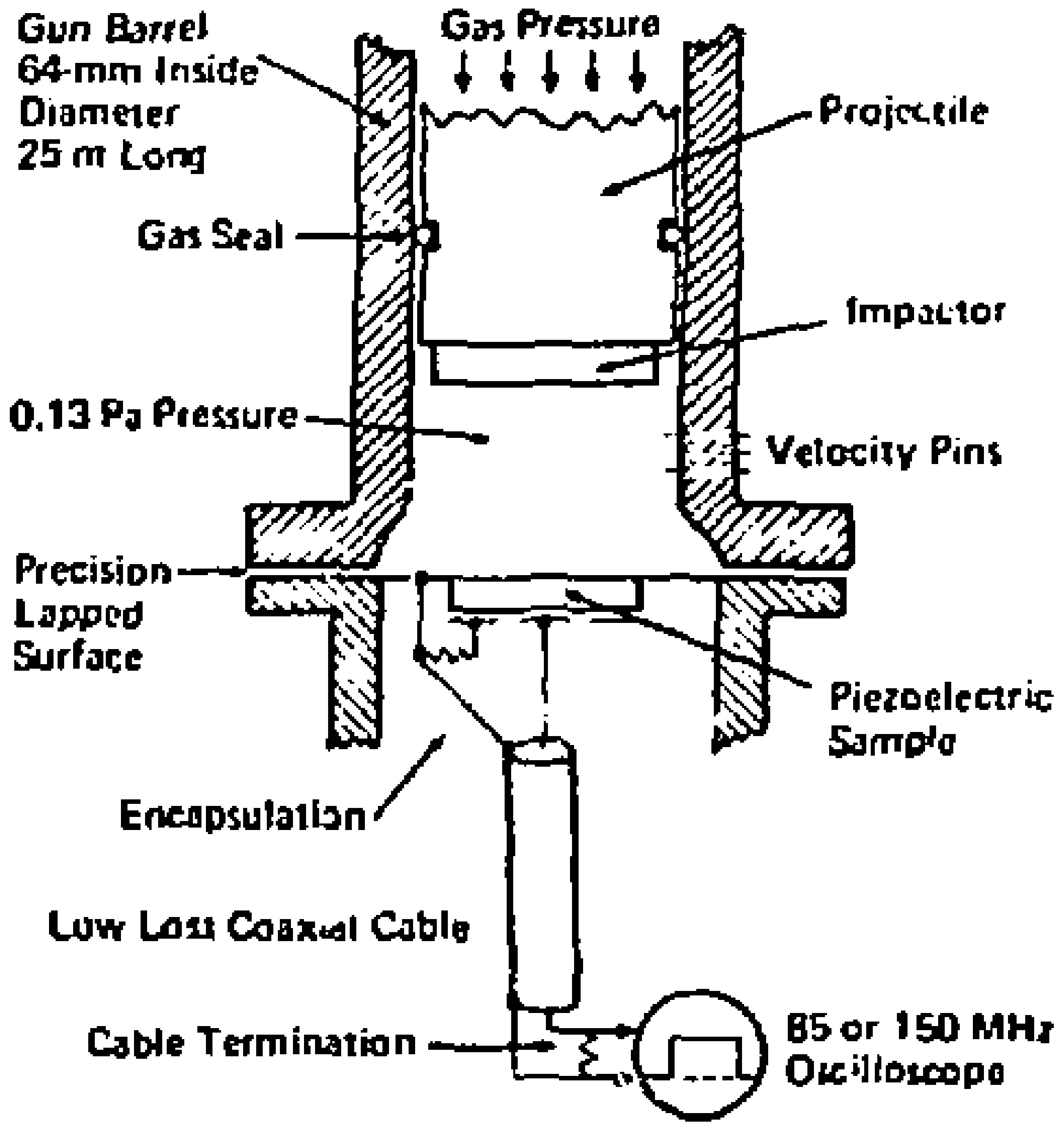

Fig. 4 Experiments to study the piezoelectric response of current-mode gage materials are conducted by accelerating a projectile to a preselected velocity, and maintaining precise alignment between the impactor and the sample. The shock wave produced by the impact propagates through the sample and produces a current which is recorded from a high speed oscilloscope. Piezoelectric characteristics are computed from the measured current, and strain is computed from the measured impact velocity and mechanical properties of the impactor and sample.

The stress or strain input to the sample can be accurately calculated from the measured impact velocity and the mechanical properties of the sample and impactor. The piezoelectric polarization can be calculated from the measured current pulse. Thus, by performing a group of experiments over a range of impact velocities, the polarization can be determined over a range of strains, and the piezoelectric constants can be obtained from the data. Since a new crystal must be used for each test (each experiment is destructive), the data provide direct evidence for the reproducibility of the piezoelectric response. The data may also be used to indicate the input stresses above which the output is no longer suitable for gage application because of distortions caused by conductivity and mechanical yielding.

Lithium niobate samples, obtained from one supplier, were cut in three different crystallographic directions. The designations for the sample orientations investigated are z-cut, y-cut, and 36-degree-rotated-y-cut (Fig. 2). Each of the crystallographic orientations has a different piezoelectric response; hence, disks cut in the different orientations may be potentially useful as gage elements for different applications.

The piezoelectric outputs of z-cut lithium niobate and x-cut quartz samples under impact loading are compared in Fig. 5. The measured piezoelectric polarization is shown for various applied compressive strains for both materials. For small strains, the linear piezoelectric constant was 1.83 C/m^2 for lithium niobate, compared to 0.17 C/m^2 for quartz. For y-cut and 36-degree-rotated-y-cut lithium niobate samples, the piezoelectric outputs were even greater, and the linearity of output with stress was good for all three materials. Table I summarizes characteristics of the different lithium niobate gages and compares them with quartz gage characteristics.

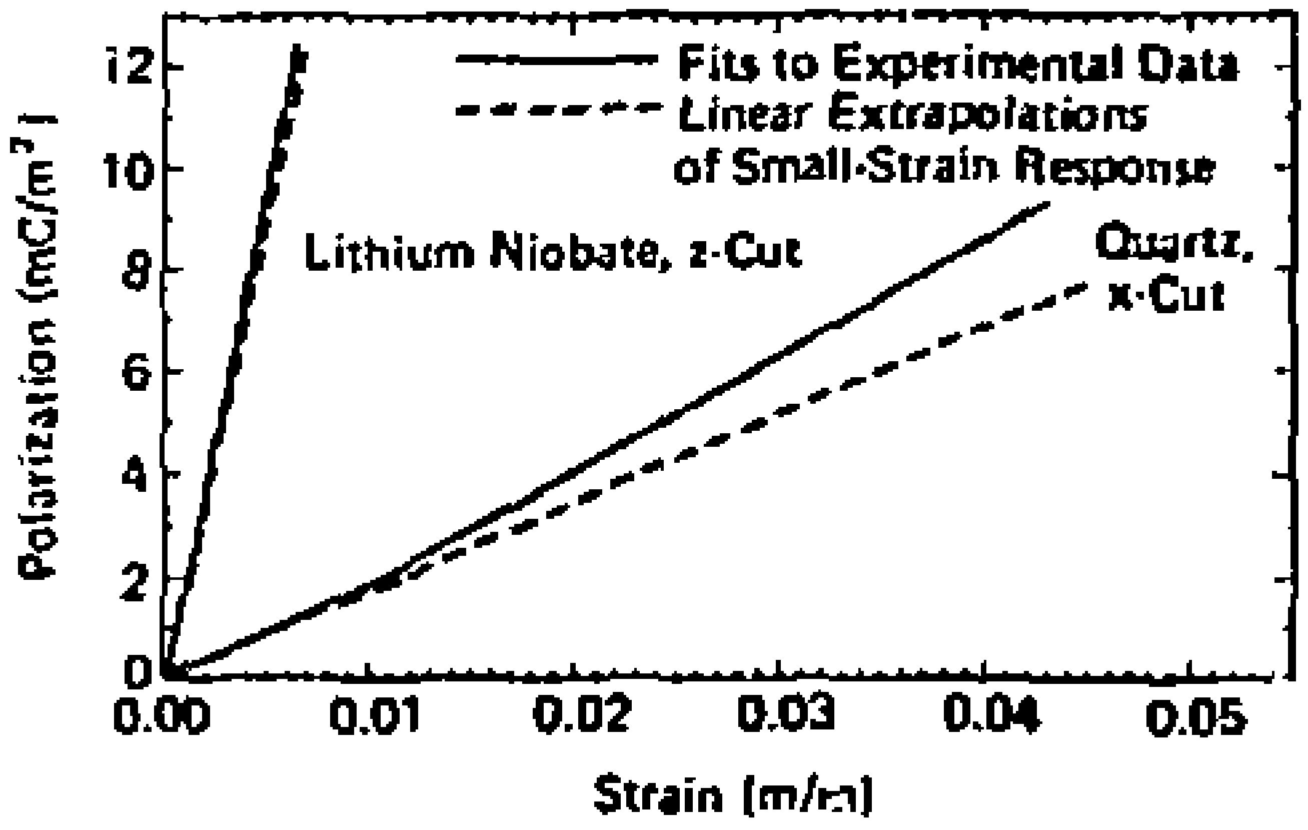

Fig. 5 The piezoelectric polarizations observed at various strains are shown for z-cut lithium niobate and compared to previous observations on x-cut quartz. The dashed lines represent an extrapolation of the linear behavior observed at small strain and the solid lines are fits to the data. The data indicate that z-cut lithium niobate has a much larger piezoelectric constant than x-cut quartz. Unacceptable distortion occurs at strain levels above those for which data are shown.

TABLE I

Current-Mode Piezoelectric Gage Characteristics

Material	Relative Sensitivity	Output Nonlinearity (% per GPa)	Distortion*	Limiting Operating Stress (GPa)
x-cut quartz	1.0	+4.8	1.04	4.0
z-cut lithium niobate	4.6	+2.5	1.08	0.8-1.4**
y-cut lithium niobate	6.5	-1.3	1.51	1.8
36-degree-rotated-y-cut lithium niobate	11.8	0	1.51	0.8

*Ratio of final current level to initial current level during transit of stress pulse from a step function input.

**Different limiting stresses are observed depending on gage thickness. The higher limits are characteristic of thicker gages.

The sensitivity of lithium niobate ranges from a factor of 4.6 to 11.8 greater than quartz. The significantly larger sensitivity permits measurements at much lower stresses or much noisier environments than possible with quartz. Alternatively, since the output signal varies directly with the area of the electrode, the use of lithium niobate makes it possible to significantly decrease the size of a current-mode gage.

The principal disadvantages of the lithium niobate gages lie in their electric current distortion and in their lower-stress operating limits. The distortion, an increase in current with time for constant applied stress, is caused by electrical-to-mechanical coupling effects. This behavior must be corrected for in order to accurately determine the stress history. We have developed a data reduction technique to remove the distortion, so this is an inconvenience but not a significant restriction.

The upper limit on the operating stress of lithium niobate, which is a consequence of shock-induced conductivity, varies from 0.8 GPa to 1.8 GPa, depending upon the sample thickness. The limit for quartz is 4.0 GPa. The lower limit for lithium niobate is a considerable disadvantage for some applications. However, there are many applications for gages in lower stress regions, where larger outputs are a distinct advantage. Since y-cut lithium niobate has a fairly high sensitivity, and the highest upper stress operating limit, it may prove to be the most useful of the three orientations.

Finally, an important result of the impact loading measurements is that the piezoelectric response of all lithium niobate samples (obtained from one supplier) was found to be highly reproducible. The measurement error associated with the equipment used in the experiments was about ±1.5%. The variation in piezoelectric response from sample-to-sample was found to be much smaller than the measurement error.

Response of Lithium Niobate to Static High Pressure

Lithium niobate exhibits a distinctive response not found in quartz: when subjected to hydrostatic pressure, a piezoelectric polarization is produced along the z-axis. To determine the linear and nonlinear hydrostatic piezoelectric constants, z-cut samples were placed in a high pressure apparatus, fluid surrounding the samples was pressurized to various levels below 2.1 GPa, and the resulting piezoelectric polarizations were measured.

The pressure-induced piezoelectric polarization was determined by connecting a one-μF capacitor across the sample and measuring the voltage on the capacitor with a high input impedance electrometer. The voltage is a direct measure of the piezoelectric polarization.

Figure 6 shows polarization data for samples from two different crystal boules of lithium niobate. The piezoelectric responses of all samples showed excellent reproducibility. The linear hydrostatic piezoelectric constant determined from the measurements was 6.31 ± 0.014 pC/m²·Pa; the output nonlinearity was -14% per GPa. Although the nonlinearity is significant, it has been well characterized, and can be compensated for in impulsive pressure measurements.

A few tests were also conducted on samples from four other suppliers. The linear and nonlinear constants were in excellent agreement with those determined from samples of the principal supplier.

Gage Development

Data obtained in this investigation were used to develop lithium niobate stress transducers for various laboratory programs. Lithium niobate disks were used to construct current-mode gages for measuring stress profiles in impact loading, pulsed electron beam, and pulsed x-ray experiments. A hydrostatic charge-mode gage was developed and used in the spark-drilling program,[4] and uniaxial charge-mode gages developed for stress measurements in soil were used in underground nuclear and chemical explosive tests. The high sensitivity and reproducibility of lithium niobate have proven to be key factors in obtaining very useful data in these tests.

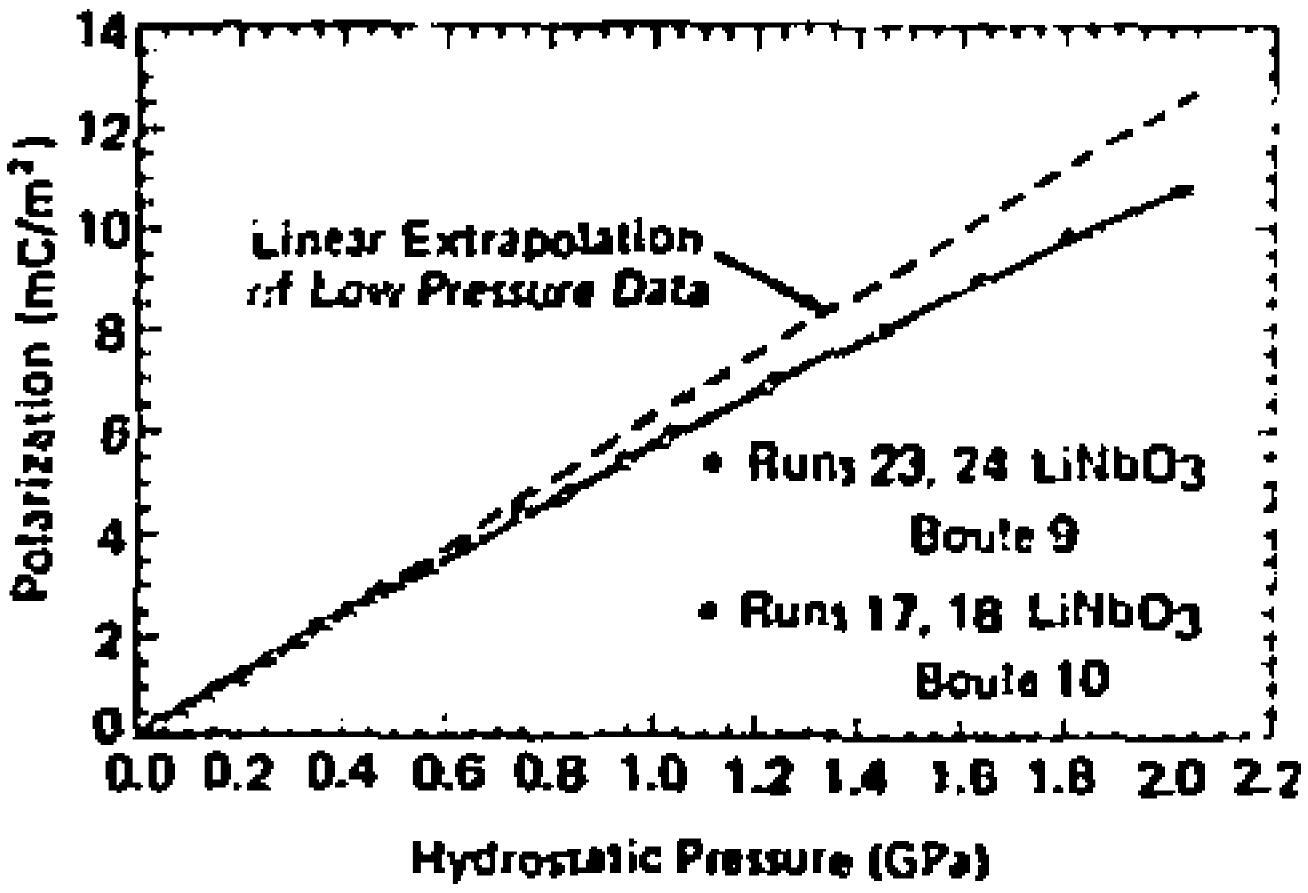

Fig. 6 The hydrostatic piezoelectric polarizations observed with two lithium niobate samples at various applied hydrostatic pressures are typical of the excellent reproducibility obtained on all the samples. The dashed line is an extrapolation of the linear behavior observed at low pressure, and the solid line is a fit to the data. The piezoelectric coefficient decreased with increasing pressure.

Conclusions

Investigation of lithium niobate to determine its piezoelectric properties has shown it to be well suited for use in piezoelectric stress transducers. Gages were developed and proven to be well adapted to measurements both in the laboratory and in the more adverse conditions in the field. From our investigation, it appears that the lithium niobate family of piezoelectric stress transducers will have a major impact on our capabilities to detect and analyze high-level transient stresses.

---

[4] *Sandia Technology*, Summer 1975, p. 33.

Stability of Liquid Films in Transpiration-Cooling

Stability characteristics of liquid films on transpiration-cooled hypersonic vehicles can be predicted by analytical models.

W. S. Saric*, K. J. Touryan

Introduction

Transpiration cooling can be used to protect a reentry vehicle from the effects of aerodynamic heating.** The technique consists of injecting a liquid coolant in the stagnation region and allowing the liquid to be swept back over the body. Liquid is removed by either entrainment or evaporation. To achieve maximum vehicle protection, the dominant liquid loss mechanism must be evaporation, since entrainment removal provides no cooling. To estimate the amount of liquid entrained by the gas, we need to determine the stability characteristics of the liquid/gas interface. For estimating the amount of liquid removal by evaporation, we need to know the roughness characteristics of the interface; that is, we need to know the interface wave characteristics such as the wavelength and amplitude.

Early subsonic experiments with a nearly incompressible gas flow showed that film instabilities occurred and that the dominant liquid removal mechanism was the entrainment of the liquid by the gas. In evaluating the concept of transpiration cooling, early investigators extrapolated the incompressible results to the supersonic case, and concluded that film instabilities would limit the effectiveness of transpiration cooling.

A systematic program was planned to develop techniques for predicting film stability characteristics and for determining wavelengths and corresponding wave velocities and amplitudes on the surface of a liquid film for both subsonic and supersonic gas flow. Models of increasing sophistication were analyzed. At each stage, the analytical results were compared with experimental observations.†

Linear Analysis

The motion of the gas parallel to the liquid layer produces two important effects on the liquid. The first is the exertion of a shear stress at the liquid gas interface, which in turn establishes a velocity profile in the liquid. The second is the exertion of pressure and shear stress perturbations on the liquid by waves on the interface. Whereas the former effect can be stabilizing or destabilizing, depending on a number of conditions, the latter effect leads to instability mechanisms.

If the external gas can be represented as inviscid and subsonic, flowing parallel to the undisturbed surface with a uniform mean velocity, the pressure perturbation is 180° out of phase with the surface wave. In this case, the gas pushes down at the troughs and sucks at the crests of the wave, thereby feeding energy to the disturbance in the liquid layer. In this model the effect of the axial component of the pressure perturbation is canceled. A different situation arises if the external flow is supersonic. In this case, the axial component of the pressure perturbation pushes at the side of the wave, giving rise to maximum energy transfer from the gas to the liquid (supersonic wave drag).

---

*Now with Virginia Polytechnic Institute.

**Technical Review, Autumn 1974, p. 28.

†Subsonic flow experiments were supported in part by the Fluid Dynamics program of the Office of Naval Research.

We analyzed two different linear models. In the first model, the external gas was assumed to be inviscid and the solution was obtained in the form of an expansion for small wave numbers (reciprocal wavelengths). In the second model, the effects of the gas viscosity and flow profile were taken into account. The disturbed boundary layer resulting from the waves was assumed to be contained in the thin laminar layer of the gas flow. The solution was obtained with a combination of a numerical technique and the "method of composite expansion" which includes the variable length-scales in the problem. The results of both models as well as other linear analyses indicated that a liquid film adjacent to a supersonic stream is much more unstable than a liquid film adjacent to a subsonic stream, a finding which is in qualitative disagreement with available data from experiments.

Description of Experiments

Four separate experimental programs were conducted in our Hypersonic Tunnel and in the New York University Hypersonic Tunnel. Flow conditions for these programs are summarized in Table I.

TABLE I

Hypersonic Tunnel Experiment Conditions

Test Series	Boundary Layer	Gas Flow
1	Laminar	Mach 5
2	Laminar	Mach 7.3
3	Laminar Turbulent	Mach 6 Mach 6
4	Laminar } Turbulent }	Mach 0.5 to 0.95 and Mach 6

The model configuration for the experiments (Fig. 1) was a sphere/cone with a 13-mm-radius hemispherical nosetip of porous stainless steel. The liquid was forced through the tip by a high-pressure expulsion system, the pressure drop across the tips being maintained between 35 and 140 MPa to prevent tunnel fluctuations and the spherical pressure distribution from affecting the flow rates.

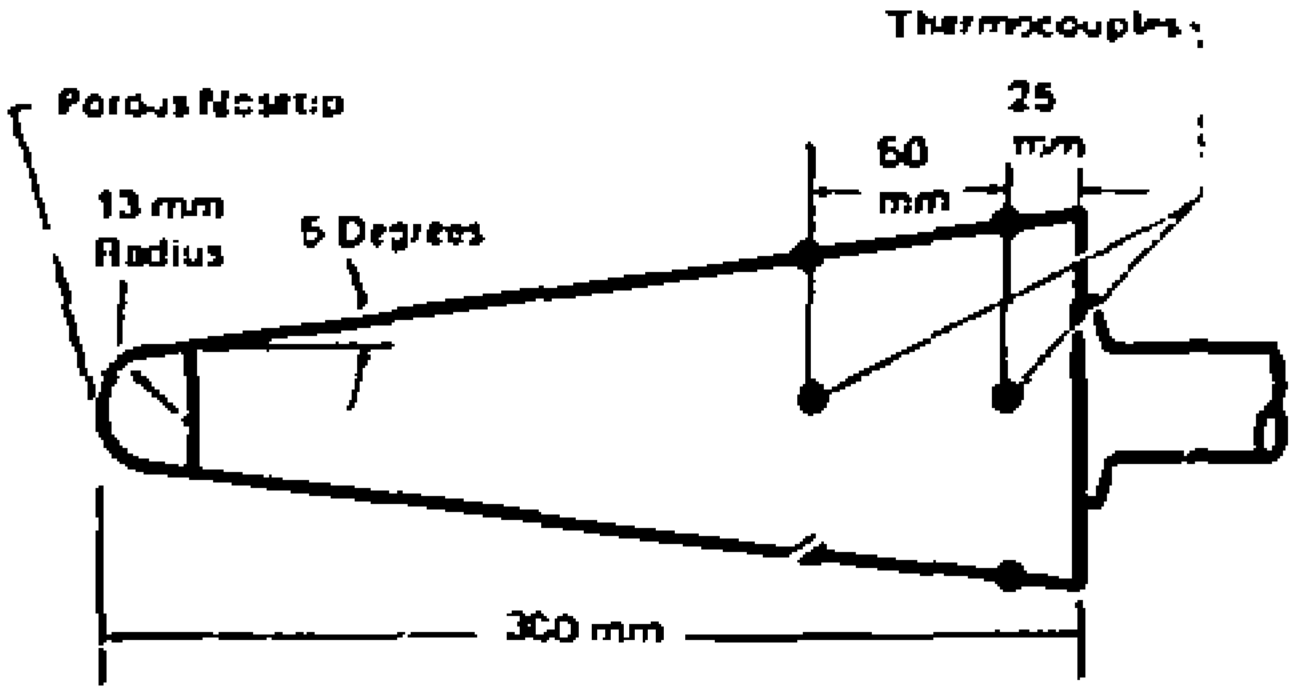

Fig. 1 Instrumented models were used in hypersonic tunnel experiments to investigate stability of liquid films on surfaces of transpiration-cooled vehicles.

The liquid flow rates were measured by recording the pressure drops across orifices that had been calibrated for fluids of different viscosities. To evaluate the gas flow conditions, we conducted tests on a dry model before each test series. The pressure and temperature measurements on the dry model permitted us to estimate the properties of the mean gas boundary layer and provided inputs to boundary layer computer codes for determining the characteristics of the mean liquid layer.

At four locations on the model, the temperature of the liquid was measured directly by thermocouples while at two other locations, the thickness of the liquid layer was measured by an "end-effect" capacitance gage developed specifically for these experiments. The output of the gage was recorded on tape, digitized, and then analyzed to obtain the mean depth of the film and the amplitude and frequency characteristics of the waves (Fig. 2).

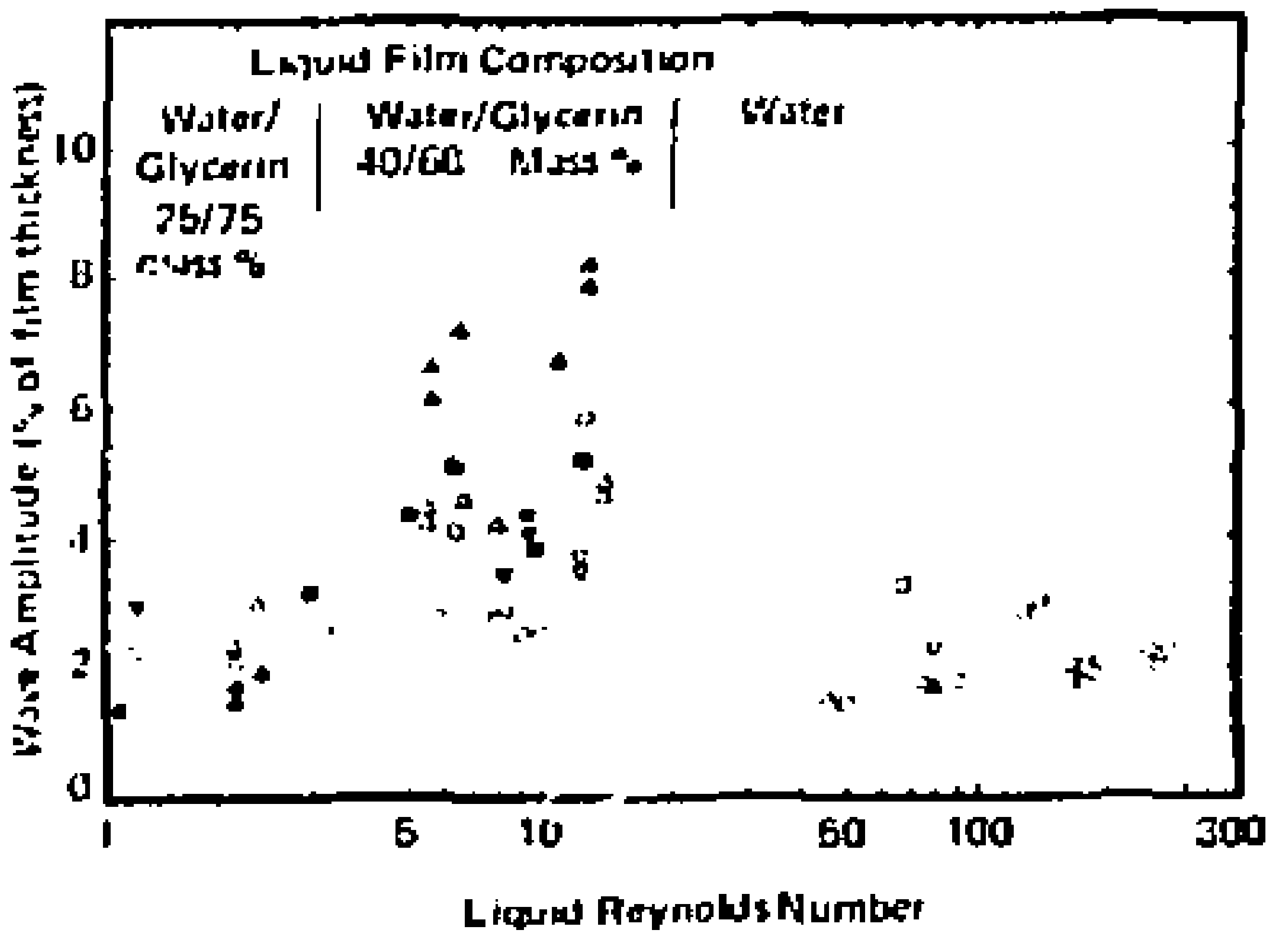

	Laminar Air Flow Measured Static Pressure (Pa)	Location		Turbulent Air Flow Measured Static Pressure (Pa)	Location
▼	8	Aft	▲	160	Aft
▼	9	Forward	▲	170	Forward
●	12	Aft	○	100	Forward
○	13.5	Forward			

Fig. 2 For a free-stream flow of Mach 6, wave amplitudes on liquid films vary with liquid flow characteristics for both laminar and turbulent air flow. The liquid Reynolds number is a dimensionless parameter that includes velocity, viscosity, and film thickness.

Spark microphotographs of the wave patterns were taken at a magnification of 100 times actual size to examine the wave profiles and to detect any liquid drops entrained in the gas boundary layer. Top and side high-speed framing cameras were used to observe response of the gas-liquid interface. Wave velocities and wavelengths were determined from the film records.

In the supersonic flow experiments, waves were observed to form on the surface of a stable liquid film. This was true for all liquid Reynolds numbers, and for both laminar and turbulent boundary layers (Fig. 3). No entrainment was observed and the mean depth measured by the capacitance gage was approximately equal to that predicted by the boundary layer code, assuming no entrainment. Furthermore, the mean amplitude decreased as the gas mean shear stress increased. For the very high shear stresses the wave amplitudes were between 2% and 5% of the mean depth. The waves were not only stable in the supersonic case, but they were not large enough (2 μm) to be called roughness elements. These experimental observations are in disagreement with the linear stability theories, which predict instability *in the supersonic case.*

Fig. 3 Waves on liquid films were found to have steady-state amplitudes for supersonic flow conditions.

For the subsonic flow experiments, linear stability parameters (laminar and turbulent boundary layers, *interface shear, gas dynamic pressure, and liquid* Reynolds number) were the same as in the supersonic flow experiments. It was observed that no liquid remained on the body in any coherent manner. The 100% entrainment observed was *vastly different from that in the supersonic flow* experiments, where no entrainment had been observed.

Nonlinear Analyses

The experimental observations can be explained by our nonlinear analyses, wherein the motion of the gas is coupled to the motion of the interface and the liquid film. Four models of increasing sophistication were analyzed:

In the first model, the liquid film was assumed to be quiescent and the gas was assumed to be inviscid, of near-zero density, and moving with a uniform velocity parallel to the liquid film. The results of this model showed that for supersonic flow, unstable linear disturbances did not grow indefinitely but attained steady-state amplitudes, while in subsonic flow the unstable linear disturbances continued to be unstable as the amplitude increased. Both behaviors were consistent with experimental observations.

In the second model, the density of the gas was included. The results of this model showed that there exists a critical gas/liquid density ratio above which unstable linear disturbances correspond to finite-amplitude stable waves and below which unstable disturbances continue to be unstable as the amplitude increases. Thus, if a gas flows subsonically parallel to a liquid surface, conditions exist for liquid entrainment by the gas according to the nonlinear theory, in qualitative agreement with the experiments.

The initial quiescent liquid assumption was removed in the third model by taking into account the liquid velocity profile (i.e., the mean shear stress exerted by the gas on the interface). However, the pressure and shear perturbations exerted by the gas on the liquid film (caused by the appearance of waves) were calculated by assuming the gas to have a uniform velocity parallel to the mean liquid film. Again, the results of this model showed that unstable linear disturbances achieve steady-state amplitudes in the supersonic case, in qualitative agreement with the experimental observations.

In spite of the success of the third model in predicting the existence of the experimentally observed periodic waves, it could not quantitatively predict the observed wavelength and its corresponding amplitude. Therefore, this model was improved by including the effects of gas viscosity and mean velocity profile in calculating the pressure and shear perturbations exerted by the gas on the gas/liquid interface. The disturbed boundary layer was assumed to be contained in the mean laminar sublayer. The disturbance equations were solved using a numerical-perturbation technique. This new model predicts the existence of steady-state periodic waves. The predicted wave numbers are found to be in good agreement with those observed over wedge- and cone-shaped models in laminar supersonic wind tunnels. Although the present analysis cannot predict the observed amplitudes, we feel that this can be done by removing the limitation that the disturbed layer be contained in the mean laminar sublayer.

Conclusions

The stability of liquid films adjacent to compressible streams has been investigated both analytically and experimentally. Linear theories predict that films adjacent to supersonic streams are much more unstable than those adjacent to subsonic streams. This is in qualitative disagreement with experimental observations. Although stability parameters were matched in the subsonic and supersonic experiments, it was found that films adjacent to supersonic streams are stable, while those adjacent to subsonic streams are unstable, as evidenced by the entrainment of the liquid by the gas. These experimental observations can be explained by our nonlinear theories which predict that linear unstable disturbances achieve steady-state amplitudes in the supersonic case and continue to be unstable in the subsonic case.

Accident-Resistant Containers for Nuclear Weapons

To prevent detonation of high explosives in accidents during transportation of nuclear weapons, we have developed a practical technology for design of accident-resistant containers.

R. E. Berry

Introduction

We are developing systems for improving safety and security during surface or air transportation of nuclear weapons. For surface transportation these goals are being accomplished with *Safe-Secure trailers and railcars, special escort* vehicles, and a dedicated digital communications system.

Air transportation accidents generate the severest impact conditions and could, potentially, result in detonation of *high explosive (HE) and dispersal of fissile material.* An accident-resistant container (ARC) has been developed that not only protects weapons in such accidents but can also be used to further improve surface transportation safety. A smaller helicopter accident-resistant container (HARC) has been developed specifically for helicopter transport of small tactical weapons in forward areas. Both designs also provide substantial protection from fragments and projectiles.

Initial design goals are summarized in Table 1.

Accident Environments

Statistics on the dominant environments, impact and fire, are shown in Figs. 1 and 2, respectively.

An analysis of Fig. 1 led to the selection of an 84 m/s impact normal to an unyielding surface as the design environment. This severity would be exceeded only in accidents such as direct flight into a mountain face. Similarly, Fig. 2 shows that attainment of a three-hour fire capability gives excellent protection in fixed-wing aircraft, helicopter, and truck accidents and even provides good protection in long-duration rail transport fires.

TABLE I

Accident-Resistant Container Design Goals

Minimize probability of HE detonation from:

- High-velocity impact of the ARC
- Extended exposure to fire
- High-velocity fragment/projectile impact on the ARC
- Detonation of HE in adjacent ARC

Container design should:

- Be compatible with most stockpile weapons
- Be compatible with current transportation carriers (air - truck - rail)
- Ensure that weapon will not be damaged in normal transportation

Additional design considerations:

- Special handling not required
- Long-term use
- Minimum maintenance and cost

The combined probability model of severity of impact velocity and fire duration is shown in Fig. 3, with point "A" illustrating that the attainment of the above goals would provide protection in at least 93% of fixed-wing cargo aircraft accidents.

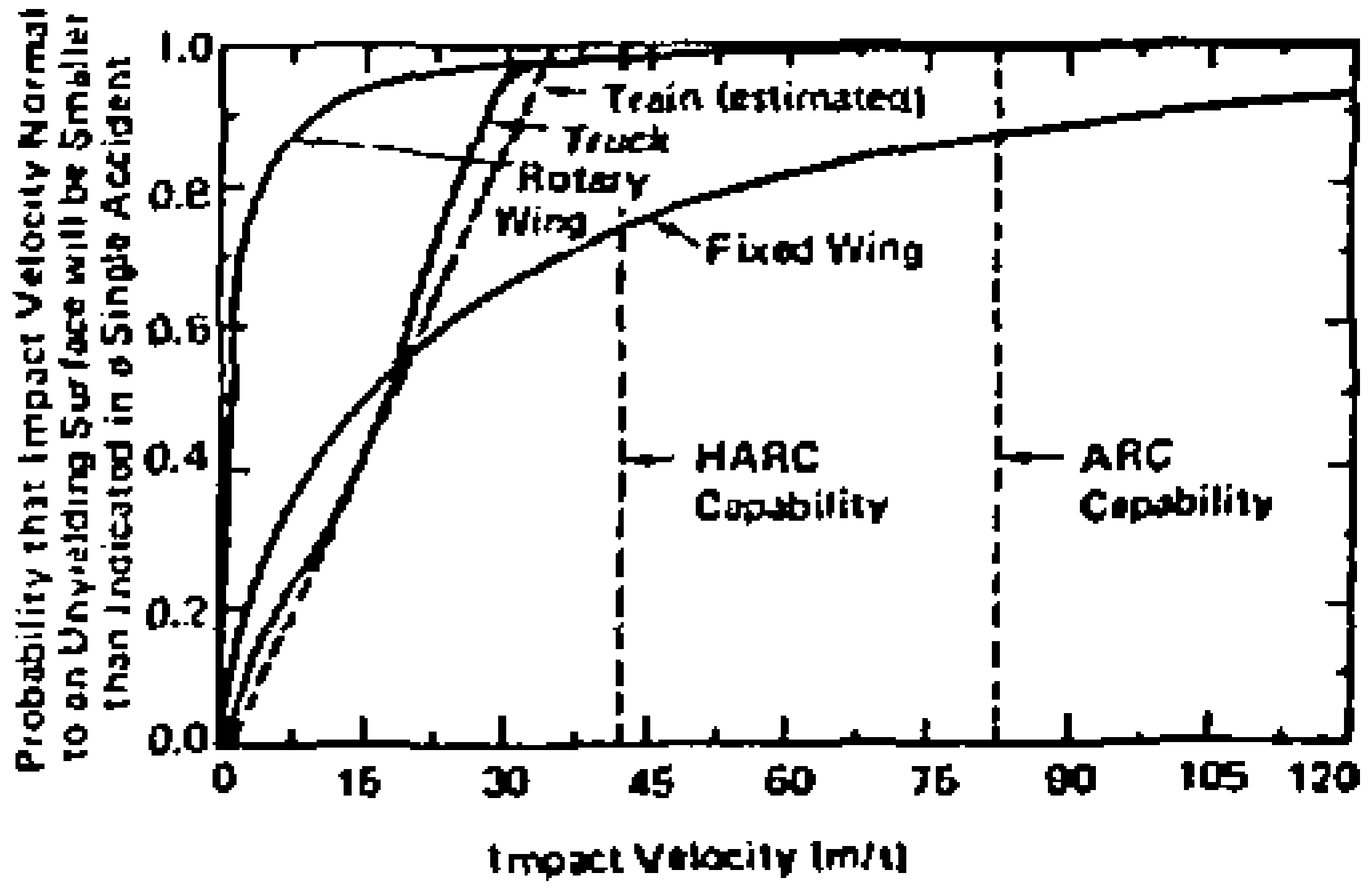

Fig. 1 Severity of impact in transportation accidents. For example, the impact velocity is smaller than 43 m/s in 75% of fixed-wing aircraft accidents, in 97% of helicopter and truck accidents, and in 100% of train accidents.

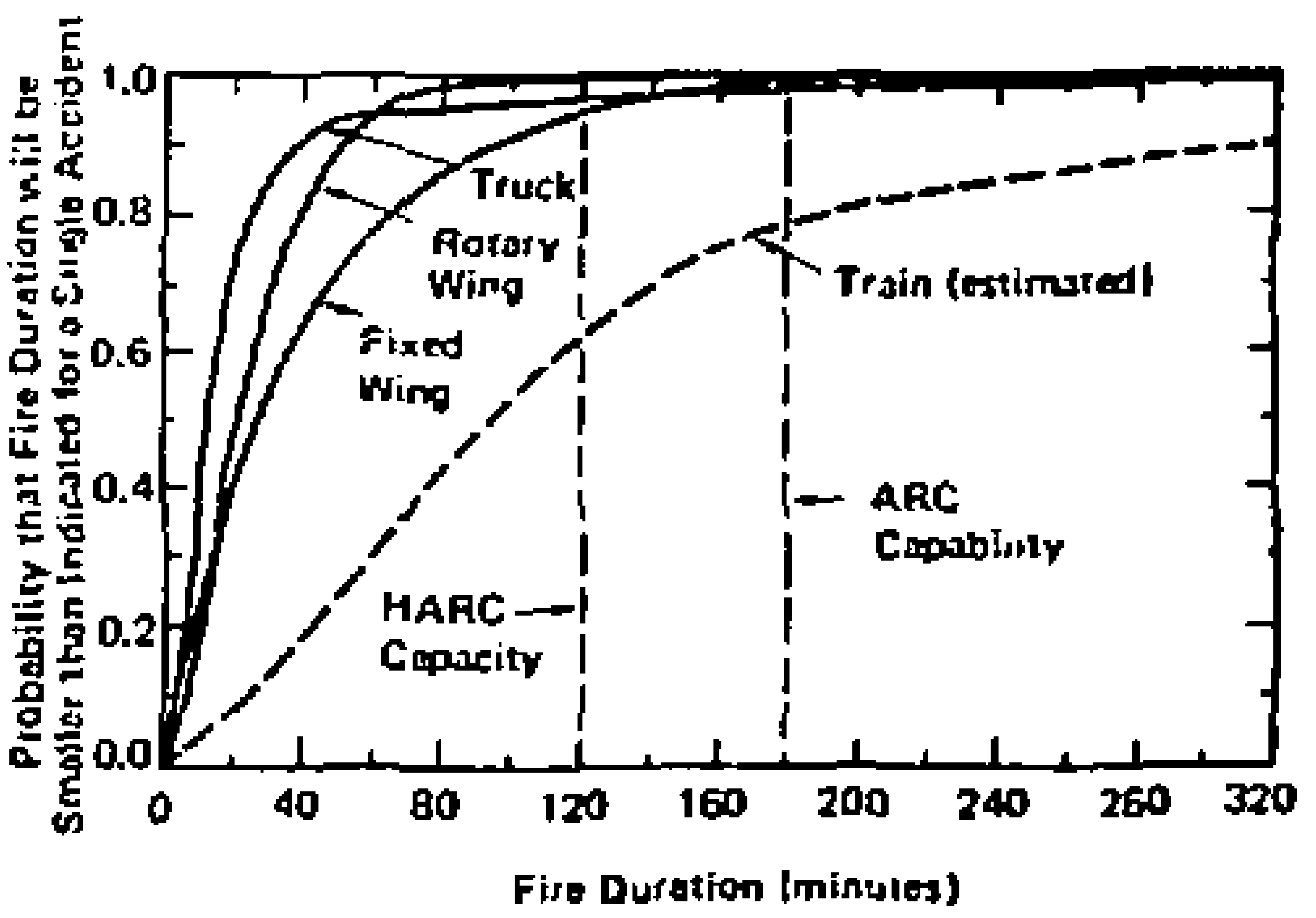

Fig. 2 Severity of fire exposure in transportation accidents.

A similar analysis for helicopter accidents produced design goals of 43-m/s-impact and 90-minute-fire-duration. A graph similar to Fig. 3, but constructed for helicopter accident environments, shows that these goals, if attained, would provide protection in more than 98% of helicopter accidents. Such a container would still provide protection in 80% of the fixed-wing accidents, as shown by point "H" in Fig. 3.

Technology Programs

The primary objectives in ARC and HARC activities were to successfully bring together the expertise and technology to analyze probable transportation accident environments, to determine the protection necessary to prevent HE detonation in weapons, to select promising materials and configurations for providing the required protection at the lowest long-term cost, and to demonstrate that the design goals could be effectively and economically achieved.

These objectives have been successfully attained. Prototype hardware of possible ARC and HARC designs has been constructed, tested, and evaluated.

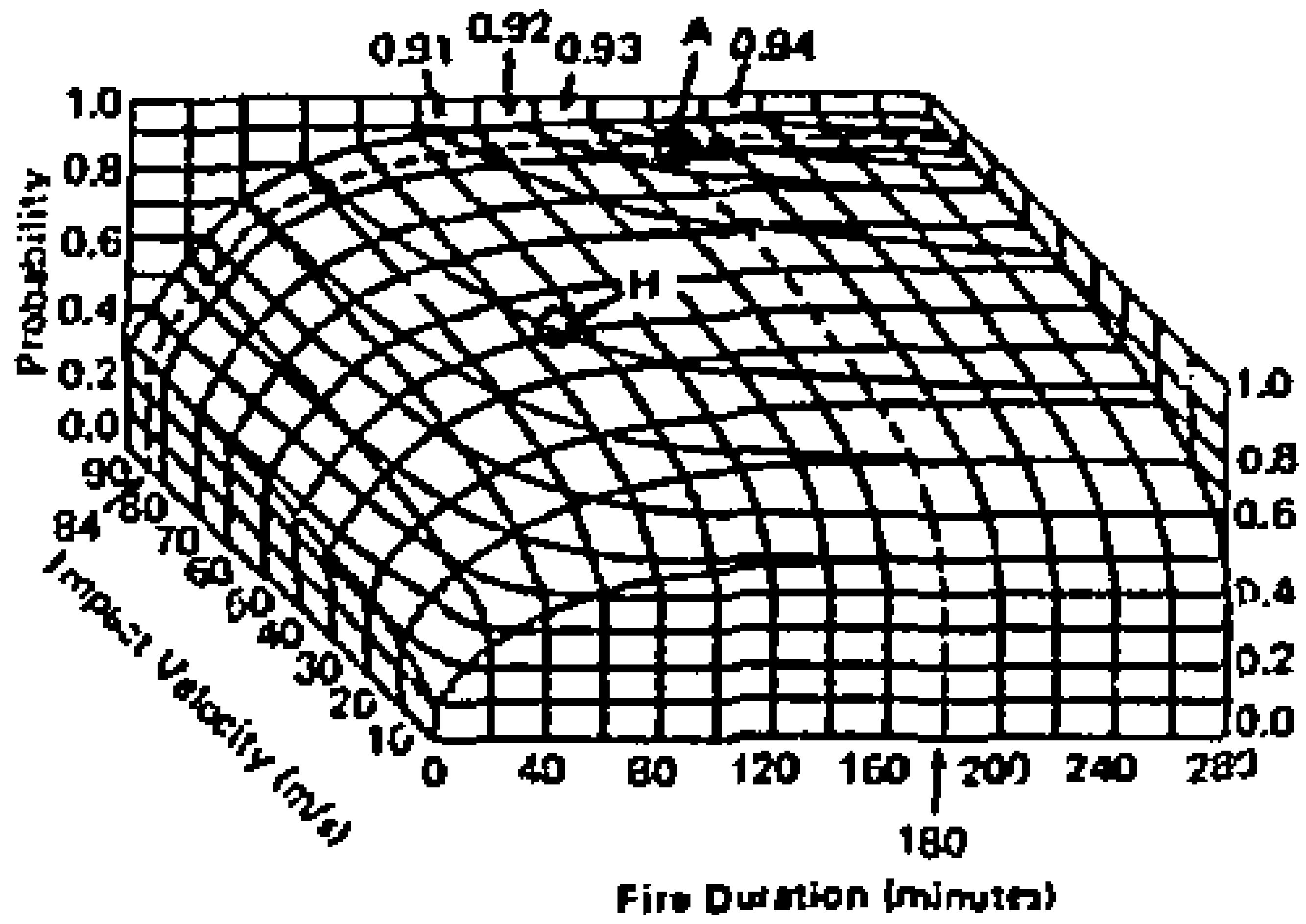

Fig. 3 Some design features of accident-resistant containers involve tradeoffs between impact resistance and fire resistance. A fire and impact accident model, represented by the curved surface, was developed from analysis of fixed-wing cargo aircraft accidents to aid in design optimization. As an example to aid interpretation, design for 84 m/s impact survival and 180-minute fire survival can be represented by point "A" on the surface. That point falls at a level of 0.93, which indicates that 93% of accident situations will involve severities no no greater than 84 m/s and 180 minutes for impact and fire, respectively. Point "H" indicates that the small HARC designed for less-severe helicopter accidents provides substantial protection even in fixed-wing aircraft accidents.

ARC Design

Protection of a nuclear weapon from crushing requires a rigid inner container that maintains its shape under all accident conditions. This rigid inner container is surrounded by an energy-absorbing structure, and enclosed in a tough steel outer shell. In the prototype design (Fig. 4) redwood is used for energy absorption, because redwood has not only excellent energy-absorption characteristics during crush, but also has low thermal conductivity and good charring characteristics when exposed to fire. When crushed in a direction parallel to the grain its strength is 37 MPa; perpendicular to the grain, its strength is 7 MPa. Grain orientation in the prototype is selected to give proper absorption *for all impact orientations. Two aluminum collars are* placed in the redwood structure to help restrain motion of the inner container *when impact is not directly parallel* or perpendicular to the axis.

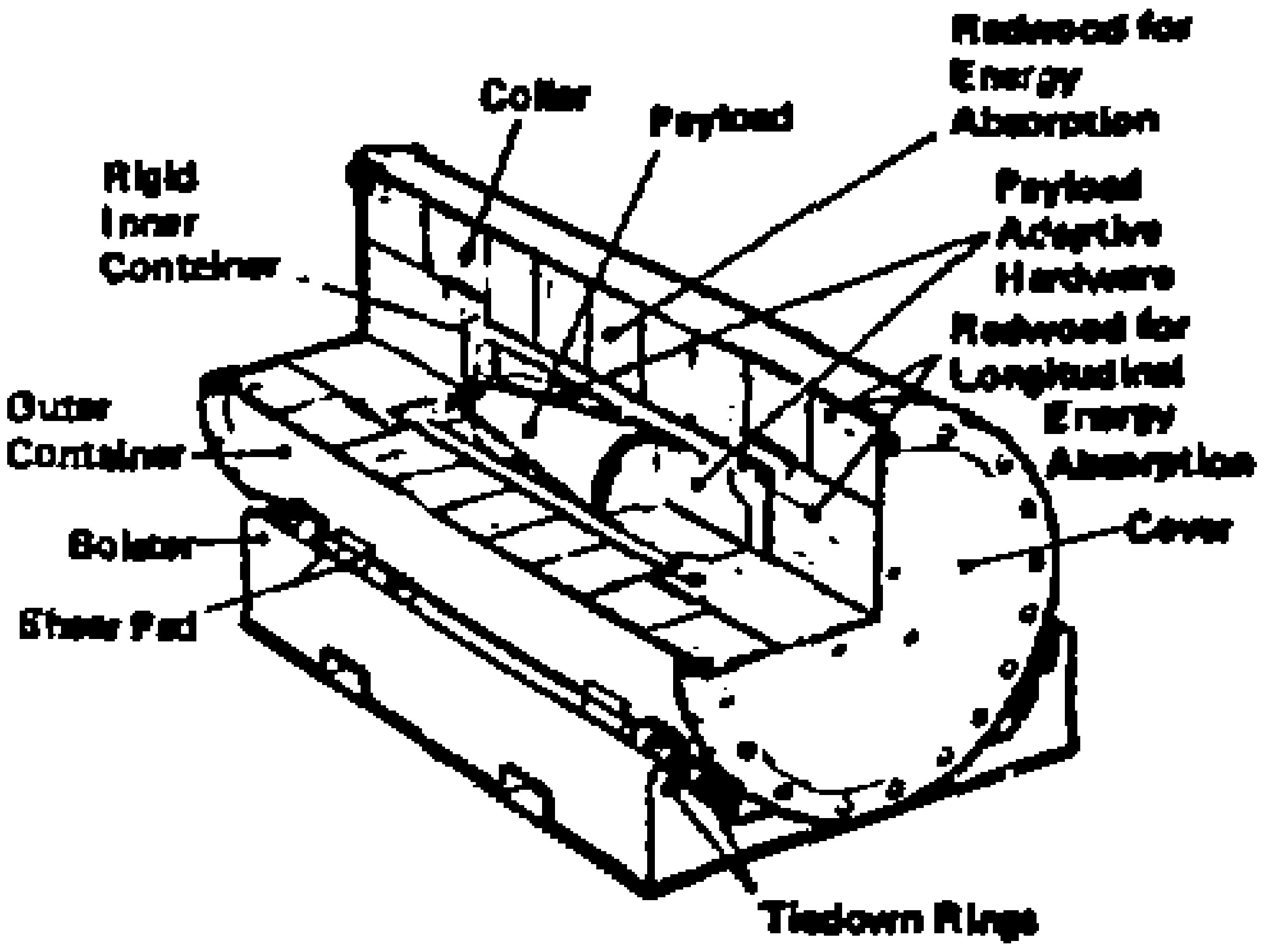

Fig. 4 An accident-resistant container (ARC) for a nuclear weapon *has structural features to absorb* energy and protect the weapon in severe transportation accidents.

The inner container, of 7075-T73 aluminum, has an inside diameter of 0.52 m, an inside length of 1.54 m, and a wall thickness of 77.5 mm. Each weapon payload to be placed in the container would have adaptive hardware that includes additional shock-mitigating material.

The outer container is HY-80 alloy steel which has a yield strength of 550 MPa, elongation of 22%, and very high fracture toughness. With the addition of a bolster, tiedown fittings, and shear attachment pads, the mass of the complete ARC is about 3400 kg. The overall structure provides some additional transportation security because the size and mass of the configuration make difficult the quick removal of the weapon without proper equipment.

The HARC designed for helicopter transport is of similar design, as shown in Fig. 5, but uses 6061-T651 aluminum for the inner container, and 304 stainless steel for the outer container. The mass of the HARC, with bolster, is 570 kg. Since the design thickness of the inner container that was adequate for rigidity was insufficient to prevent penetration by 7.62-mm (caliber .30) armor-piercing (AP) projectiles, the thickness was increased to 35 mm. To accommodate payloads, the inner container has an inside diameter of 0.406 m and an inside length of 1.03 m.

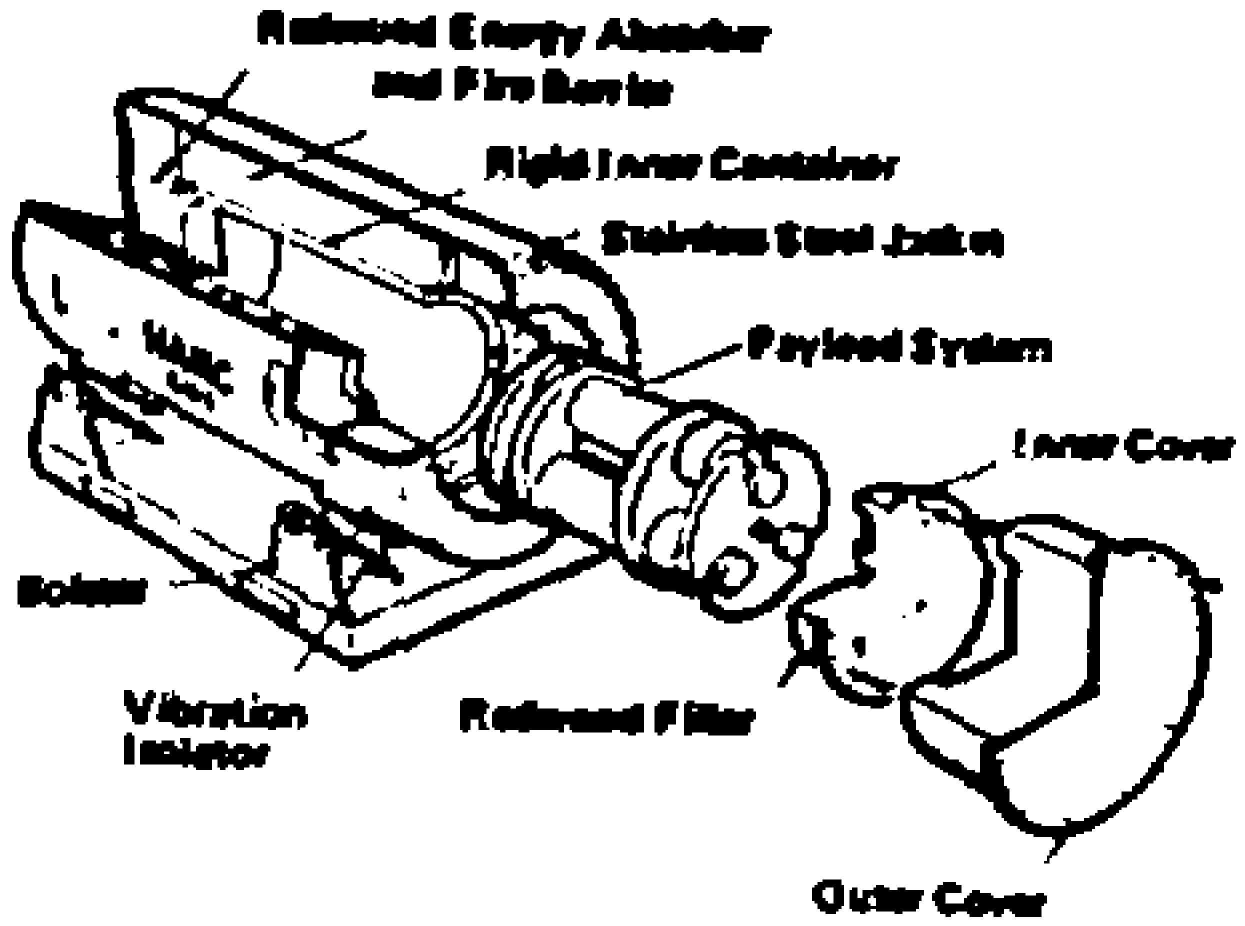

Fig. 5 An accident-resistant container (HARC) for small tactical weapons can be transported by helicopters in forward areas.

ARC Testing

ARC evaluation tests have included high-velocity impacts at various impact angles, fuel-fire exposure, radiant-heat exposure, and some projectile-impact and explosive-destruct experiments. Most of these tests were with quarter-scale model hardware. Impact evaluation of eight full-size prototype ARC's has shown that the design will survive the high-velocity impact environment. Models in the tests indicate that the ARC will also survive the design fire environment. Full-scale tests with 7.62 mm and 12.7 mm (caliber .50) AP projectiles impacting flat panels indicate that neither will penetrate the ARC.

A full-scale test for sympathetic detonation between ARC's was conducted with actual weapons (less fissile material). Intentional detonation of the HE in one ARC resulted in little damage to the weapon in the adjacent ARC.

One warhead design with simulated HE was evaluated in five full-scale prototype ARC impact tests at different impact angles. In four of the five tests, results indicated that live HE would not have detonated. One of these successes was a repeat of an earlier test that had indicated a deficiency in the adaptive hardware design which was subsequently corrected.

The preferred orientation for ARC shipment is with the longitudinal axis parallel to the aircraft longitudinal axis. This orientation would result in end-on impact in most accidents. Nuclear weapons, in general, are more resistant to impact along their longitudinal axis than along their lateral axes. The forward end of the nuclear weapon warhead is normally more resistant to impact than the aft end and therefore, an ARC with a forward-oriented weapon offers the highest probability of warhead HE survival in an aircraft accident.

The HARC has also been evaluated with model hardware. Impact and fire tests indicate that HE would not be detonated for impact velocities of 43 m/s and fire durations of two hours. Full-size sections successfully prevented penetration of 7.62 mm AP projectiles. A range of evaluation tests of full-scale HARC systems is being completed.

Conclusions

We have successfully designed a container (ARC) which will prevent, in 95% of fixed-wing cargo aircraft accidents, detonation of nuclear weapon high explosives. A similar container design (HARC) can protect weapons in 98% of helicopter accidents. The design trade-offs are sufficiently understood to permit tailoring of the design to provide any appropriate level of protection. The same technology is also applicable to nonweapon containers for special nuclear materials. This technology is now on-the-shelf and available to greatly improve safety in both air and surface transportation.

METRICATION

The Système International d'Unités (SI) is a modernized metric system that is the world's common language for expressing scientific and technical data. It is a coherent system that uses seven base units: metre (m) for length, kilogram (kg) for mass, second (s) for time, kelvin (K) for thermodynamic temperature, ampere (A) for electric current, mole (mol) for amount of substance, and candela (cd) for luminous intensity. Two supplementary units are defined: radian (rad) for plane angle and steradian (sr) for solid angle. Many derived units are defined from the base and supplementary units. These include newton (force), joule (energy, work), pascal (pressure, stress), hertz (frequency), watt (power), and many electrical and photometric units. Below are conversion factors for quantities of special interest.

LENGTH	1 in.	= 25.4 mm (millimetres) = 0.0254 m
	1 ft	= 0.3048 m (metres) = 304.8 mm
	1 Å	= 0.1 nm (nanometre) = 1 x 10^{-10} m
MASS	1 lbm	= 0.454 kg (kilograms)* = 454 g
FORCE	1 lbf	= 4.448 N (newtons)*
ENERGY	1 cal	= 4.184 J (joules)
	1 keV	= 0.160 fJ (femtojoules)* = 0.160 x 10^{-15} J
	1 Btu	= 1054.350 J (joules)* ≈ 1.054 kJ
PRESSURE and STRESS	1 psi	= 6.895 kPa (kilopascals)* = 6895 Pa
	1 torr (mm Hg)	= 0.133 kPa (kilopascals)* = 133 Pa
	1 bar	= 0.1 MPa (megapascals) = 1 x 10^5 Pa
POWER	1 hp	= 746 W (watts)
VOLUME	1 yd^3	= 0.765 m^3 (cubic metres)*
	1 gal	= 3.785 ℓ (litres)* = 0.003785 m^3
DENSITY	1 g/cm^3	= 1 Mg/m^3 (megagram per cubic metre) = 1 x 10^3 kg/m^3
	1 lbm/ft^3	= 16.018 kg/m^3 (kilogram per cubic metre)*
IMPULSE	1 ktap (1000 dyn · sec/cm^2)	= 0.1 kPa · s (kilopascal · seconds) = 100 Pa · s
TEMPERATURE	°C	= K - 273.15

*Rounded to three decimal places.

SI includes a set of prefixes that can be combined with the names of the units to indicate multiples and submultiples.

E(exa) = 10^{18}
P(peta) = 10^{15}
T(tera) = 10^{12}
G(giga) = 10^9

M(mega) = 10^6
k(kilo) = 10^3
m(milli) = 10^{-3}
μ(micro) = 10^{-6}

n(nano) = 10^{-9}
p(pico) = 10^{-12}
f(femto) = 10^{-15}
a(atto) = 10^{-18}

The use of c (centi) for 10^{-2}, while allowed in SI, is discouraged.